

## Annual Report to



---

# Using Single-Molecule Imaging System Combined with Nano-fluidic Chip to Understand Fluid Flow in Tight and Shale Gas Formation Project Number: 09122-29

---

Feb. 12th, 2013

PI: Dr. Baojun Bai (baib@mst.edu)

Completed by Baojun Bai, Yinfu Ma, Xiaolong Yin, Keith B.  
Neeves, Qihua Wu, Jeong Tae Ok, Yongpeng Sun

161 McNutt Hall, 1400 N. Bishop Ave.  
Rolla, MO 65409

Tel: 573-341-4016

<http://web.mst.edu/~baib>

## LEGAL NOTICE

This report was prepared by Baojun Bai as an account of work sponsored by the Research Partnership to Secure Energy for America (RPSEA). Neither RPSEA, members of RPSEA, the National Energy Technology Laboratory, the U.S. Department of Energy, nor any person acting on behalf of any of these entities:

- a. MAKES ANY WARRANTY OR REPRESENTATION, EXPRESS OR IMPLIED WITH RESPECT TO ACCURACY, COMPLETENESS, OR USEFULNESS OF THE INFORMATION CONTAINED IN THIS DOCUMENT, OR THAT THE USE OF ANY INFORMATION, APPARATUS, METHOD, OR PROCESS DISCLOSED IN THIS DOCUMENT MAY NOT INFRINGE PRIVATELY OWNED RIGHTS, OR
- b. ASSUMES ANY LIABILITY WITH RESPECT TO THE USE OF, OR FOR ANY AND ALL DAMAGES RESULTING FROM THE USE OF, ANY INFORMATION, APPARATUS, METHOD, OR PROCESS DISCLOSED IN THIS DOCUMENT.

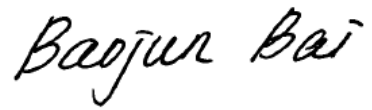
THIS IS A FINAL REPORT. THE DATA, CALCULATIONS, INFORMATION, CONCLUSIONS, AND/OR RECOMMENDATIONS REPORTED HEREIN ARE THE PROPERTY OF THE U.S. DEPARTMENT OF ENERGY.

REFERENCE TO TRADE NAMES OR SPECIFIC COMMERCIAL PRODUCTS, COMMODITIES, OR SERVICES IN THIS REPORT DOES NOT REPRESENT OR CONSTITUTE AN ENDORSEMENT, RECOMMENDATION, OR FAVORING BY RPSEA OR ITS CONTRACTORS OF THE SPECIFIC COMMERCIAL PRODUCT, COMMODITY, OR SERVICE.

**Blank page**

## Signature page

Baojun Bai, Principal Investigator

A handwritten signature in black ink that reads "Baojun Bai". The script is cursive and fluid, with the first name "Baojun" and last name "Bai" written in a single continuous line.

Date: February 15, 2013

## ABSTRACT

Gas in tight sand and shale exists in underground reservoirs with microdarcy ( $\mu\text{D}$ ) or even nanodarcy permeability ranges; these reservoirs are characterized by small pore throats and crack-like interconnections between pores. The size of the pore throats in shale may differ from the size of the saturating fluid molecules by only slightly more than one order of magnitude. The physics of fluid flow in these rocks, with measured permeability in the nanodarcy range, is poorly understood. Knowing the fluid flow behavior in the nano-range channels is of major importance for stimulation design, gas production optimization and calculations of the relative permeability of gas in tight sand and shale gas systems. The project targets on improving the understanding of the flow behavior of natural gas and introduced fluids (water, surfactant solutions and polymers) in nano-darcy range of tight sand and shale formations by using advanced single-molecule imaging system combined with nano-fluidic chips and pore-scale numerical simulation techniques. This report describes our second year's effort for the three- year RPSEA funded research project.

The first batch of nanofluidic chips with 100 nm channels fabricated in the first project year have been successfully used to run multiphase flow experiments. In addition, a new batch of nanofluidic chips has been fabricated to further the progression of experiments. The new chips have a range of characteristic pore sizes from 30 nm to 500 nm, making it possible to systematically study the effect of pore size on flow and transport properties. A lab-on-chip approach for direct visualization of the fluid flow behavior in nanochannels was developed using an advanced single-molecule imaging system combined with a nano-fluidic chip. Two phase flow behavior in nanochannels was investigated and displacement of two-phase flow in 100 nm depth channels was characterized. On numerical modeling, programs for the simulation of heat and solute transfer in porous media made up by sphere packings have been developed. The tortuosities of two dimensional random porous media models, which have been used in the experiments, have been calculated. These methods are currently being implemented to the established three-dimensional parallelized pore-scale simulation framework. Finally, to extend the capability of the pore-scale simulation to the slip flow regime, a preliminary work has been conducted to obtain the analytical solutions and the results are included in this annual report.

## TABLE OF CONTENTS

ABSTRACT.....	1
TABLE OF CONTENTS .....	2
LIST OF FIGURES.....	5
LIST OF TABLES.....	7
EXECUTIVE SUMMARY.....	8
1. NanoFluidic chips construction.....	10
1.1 Nanofluidic Chips .....	10
1.2 Microfluidic Experiments on Water-Oil Multiphase Flows.....	11
1.3 Conclusions and Future Work .....	16
2. Nano-fluidic chip experiments to understand fluid flow in nano-scale pore spaces and cracks .....	17
Part I. Development of optic imaging method for single and two-phase pressure driven flows in nanochannels .....	17
2.1 Introduction .....	17
2.2 Experimental methods.....	18
2.2.1 Materials.....	18
2.2.2 Micro-/Nano-model preparation .....	18
2.2.3 Experimental setup .....	19
2.3 Results and discussion .....	20
2.3.1 Flow rate determination and single phase flow in nanochannels.....	20
2.3.2 Two phase flow regime map in the nanochannels.....	24
2.4 Conclusions.....	28
Part II. Gas/fluid flow behavior in the nanochannels.....	28
2.5 Introduction .....	28
2.6 Experimental method.....	29
2.6.1 Materials.....	29
2.6.2 Experimental procedure .....	30
2.7 Result and discussion .....	31

2.7.1 Theory.....	31
2.7.2 Gas displacing water and two phase gas slippage effect in nanochannels .....	33
2.7.3 Water displacing gas in nanochannels .....	38
2.8 Conclusions.....	39
2.9 Future experimental plan.....	39
3. The Flow Behavior of Friction Reducer in Microchannels during Slickwater Fracturing.....	40
3.1 Summary .....	40
3.2 Introduction .....	40
3.3 Experiment .....	41
3.3.1 Materials.....	41
3.3.2 Equipment.....	42
3.3.3 Procedure .....	43
3.4 Results and discussion .....	43
3.4.1 Friction reducer solution emulsion particle size analysis .....	44
3.4.2 Concentration effect on pressure gradient and apparent viscosity .....	44
3.4.3 Effect of microchannel size on pressure gradient and apparent viscosity .....	45
3.4.4 Wettability effect on pressure gradient and apparent viscosity .....	47
3.4.5 Shear rate effect on pressure gradient and apparent viscosity .....	49
3.4.6 Residual resistance factor to water.....	50
3.4.7 Data comparison with flow loop experiment.....	51
3.4.8 Potential impact of FR solution on the shale matrix .....	51
3.5 Conclusions.....	52
Appendix.....	53
3.6.1 Appendix A.....	53
3.6.2 Appendix B.....	53
3.6.3 Appendix C .....	54
3.6 Nomenclature.....	55
3.7 Unit Conversion .....	55
4. Numerical Simulation.....	56
4.1 Summary .....	56

4.2 Tracer-Based Transport Simulations .....	56
4.3 Direct Solution of the Transport Equation and Tortuosity .....	57
4.4 Analytical and Numerical Solutions for Slip Flows in Simple Geometries .....	59
4.5 Conclusions and Future Work .....	63
5 Technology Transfer Efforts.....	66
5.1 Project Website .....	66
5.2 Full papers.....	66
5.3 Oral Presentations.....	67
5.4 Posters.....	68
5.5 Graduate thesis.....	68
REFERENCES.....	69
LIST OF ACRONYMS AND ABBREVIATIONS .....	76



## LIST OF FIGURES

Figure 1-1: Electron micrographs of silicon parts after forming micro- and nanochannels by two-steps of reactive ion etching. ....	11
Figure 1-2: Eight of the eleven pore geometries studied for water flooding and surfactant flooding are presented here.....	13
Figure 1-3: Water flooding coverage at the points of breakthrough.....	14
Figure 1-4: Displacement efficiency in chip D (water flooding – first row; surfactant flooding – second row) and in chip V (water flooding – third row; surfactant flooding – fourth row).....	15
Figure 1-5: Recovery factor at of chips U~TV at points of break-through.....	15
Figure 2-1: Fluid transport system and schematic of the nanofluidic chip.....	20
Figure 2-2:Comparisons between experimental results and theoretical results of intensity changes with different fluorescence dye concentration.....	22
Figure 2-3: Average volumetric flow rate vs. pressure drop in a nanochannel. ....	24
Figure 2-4: Water/gas two phase flow patterns in nanochannels. ....	26
Figure 2-5: Water/gas two phase flow regime map in nanochannels .....	27
Figure 2-6: Schematic of nanochannel array as the experimental test section .....	30
Figure 2-7: Flow patterns of immiscible two phase flow in nanochannel.....	34
Figure 2-8: Measurement of gas permeability at different water saturation, step 1. ....	35
Figure 2-9: Measurement of gas permeability at different water saturation, step 2. ....	35
Figure 2-10: Measurement of gas permeability at different water saturation, step 3...35	
Figure 2-11: Gas slip effect at different water saturations.....	36
Figure 2-12: Correlation between water saturation and gas slip factor. ....	37
Figure 2-13: Distribution of water saturation in nanochannels.....	38
Figure 2-14: Water displacing gas patterns, two different interfaces patterns. ....	39
Figure 3-1: Microchannel cross-sectional diameter examined with SEM. ....	41
Figure 3-2: Schematic diagram of experiment. ....	43
Figure 3-3: Particle size distribution of 0.05 vol% FR solution.....	44
Figure 3-4: Effect of FR solution concentration. ....	45
Figure 3-5: Effect of microchannel size. ....	46
Figure 3-6: Reynolds number vs. velocity.....	47

Figure 3-7: Wettability effect. ....	48
Figure 3-8: Apparent viscosity difference vs. velocity under different wettabilities.....	48
Figure 3-9: Boundary layer change with velocity. ....	49
Figure 3-10: Shear rate effect on apparent viscosity. ....	49
Figure 3-11: Residual resistance factor of different microchannels.....	51
Figure 3-12: Resistance factor vs. flux for 600 ppm Xanthan.....	53
Figure 3-13: Resistance factor vs. shear rate for 600 ppm Xanthan.....	53
Figure 3-14: Blood flows in different gaps between the shearing plates. ....	54
Figure 4-1: A schematic of the tracer algorithm showing the advection-diffusion process of tracers and implementation of specular reflection on a pore wall.....	57
Figure 4-2: Axial velocity distribution of a flow through a packing of spheres (upper left). ....	57
Figure 4-3: Geometry models used for tortuosity calculation. ....	58
Figure 4-4: Porosity-tortuosity relations for two-dimensional porous media geometry models presented in Figure 4-3. ....	59
Figure 4-5: Estimates of the Knudsen number at various pressures for four given pore sizes.....	60
Figure 4-6: A cylinder placed in the center of a square domain for COMSOL simulation and the finite element grid. The force density is applied such that the flow is from left to right. The dimensions are in the unit of micrometers.....	61
Figure 4-7: Effect of Knudsen number on the ratio/ from COMSOL simulations.....	62
Figure 4-8: Effect of slip on the velocity profile in a 2D Fracture – Analytical solution. ....	64
Figure 4-9: Velocity profile of no-slip flow (top) and slip flow (bottom) in a nanofluidic channel (100 nm x 5 $\mu$ m).....	65

## LIST OF TABLES

Table 1-1: Permeability of the microfluidic chips. ....	12
Table 1-2: Fluids used in the drainage experiments and their properties.....	13
Table 2-1: Flow regime based on Knudsen number.....	32
Table 3-1: Microchannel Parameters .....	42
Table 3-2: Time to reach equilibrium .....	46
Table 3-3: Permeability to capillary diameter conversion .....	53

## EXECUTIVE SUMMARY

This project focuses on clarifying the flow behavior of natural gas and introduced fluids (water, surfactant solutions and polymers) in micro-fractures and nano-sized pores of tight sand and shale formations by using an advanced single-molecule imaging system combined with nano-fluidic chips and pore-scale numerical simulation techniques. This report describes our second year's effort for the three-year RPSEA funded research project.

**NanoFluidic chips construction.** The first batch of nanofluidic chips with 100 nm channels fabricated in the first year have been successfully used to run multiphase flow experiments. A new batch of nanofluidic chips has been fabricated to further the progression of experiments. The new chips have a range of characteristic pore sizes from 30 nm to 500 nm, making it possible to systematically study the effect of pore size on flow and transport properties. Microfluidic chips were used to conduct water flooding and surfactant flooding experiments on chips with random pore size distributions and/or vugs, and the effect of pore structure on displacement efficiency was characterized.

**Development of optic imaging method for single and two-phase pressure driven flows in nanochannels.** A novel lab-on-chip approach for direct visualization of the fluid flow behavior in nanochannels was developed using an advanced single-molecule imaging system combined with a nano-fluidic chip. Experiments of single and two phase flow in nanochannels with 100 nm depth were conducted. The linearity correlation between flow rate and pressure drop in nanochannels was obtained and fit closely into the Poiseuille's Law. Meanwhile, three different flow patterns, single, annular, and stratified, were observed from two phase flow in nanochannels experiments and their special features were described. A two-phase flow regime map for nanochannels was presented.

**Gas/liquid fluid flow behavior in the nanochannels.** Displacements of two-phase flow in 100 nm depth channels were characterized. Specifically, the two-phase gas slippage effect was investigated. Under experimental conditions, the gas slippage factor increased as the water saturation increased. The two-phase flow mechanism in nanochannels was proposed and proved by the flow pattern images. The results are crucial for permeability measurement and gas slippage factor determination for unconventional shale gas systems with nano-scale pores.

**The Flow Behavior of Friction Reducer in Microchannels during Slickwater Fracturing.** Friction reducer (FR) is the primary component of hydraulic fracturing fluid. It can decrease the flowing friction in the tubing of wellbore. Lab tests and field applications have addressed this issue thoroughly. However, the flow characteristics of this solution in microfractures are not clear. We studied the

flow behavior of the solution through capillary tubes with different diameters. The effects of solution concentrations, capillary tube diameter and wettability on injection pressure were investigated in details. Finally, the experimental results were compared with field data, and the impact of friction reducer on the shale gas formation damage was analyzed.

**Pore-scale Numerical Simulation.** We wrote tracer-based algorithms for heat and mass transfer in random geometries made up by spheres. We also calculated the tortuosity of two-dimensional random porous media models made up by channels using lattice-Boltzmann-based methods. These methods are currently being implemented to the established three-dimensional parallelized lattice Boltzmann framework. Finally, to extend the capability of the lattice Boltzmann to the slip flow regime, a preliminary work has been conducted to obtain the analytical solutions and the results are included in this annual report.

## 1. NanoFluidic chips construction

**Summary:** The objective of this work is to fabricate nanofluidic chips to enable study of multiphase flow on a length scale more relevant to the size of pores in tight sand and shale formations. We successfully fabricated microfluidic and nanofluidic networks using PDMS, silicon, and quartz. The first batch of nanofluidic chips with 100 nm channels fabricated in the first project year have been successfully used to conduct multiphase flow experiments. Another batch of nanofluidic chips was fabricated to further the progression of experiments. The new chips have a range of characteristic pore sizes from 30 nm to 500 nm, making it possible to systematically study the effect of pore size on flow and transport properties. On microfluidic chips, we conducted water flooding and surfactant flooding experiments on chips with random pore size distributions and/or vugs, and the effect of pore structure on displacement efficiency was characterized.

### 1.1 Nanofluidic Chips

New batches of nanofluidic devices with a series of parallel channels ( $100\text{ nm} \times 5\text{ }\mu\text{m}$ ) were fabricated and used to visualize two-phase flow. These devices consist of relief patterns etched in silicon and a transparent glass top [1]. More recent efforts have focused on the fabrication of nanofluidic channels with more complex and varying geometries (Figure 1-1). First, a series of devices were fabricated in order to determine the effect of channel depth on fluid displacement. In that, a set of parallel channels were fabricated with depths of 50 nm to 500 nm and a constant depth-to-width aspect ratio of 1: 50. Second, random porous media analogs were created based Voronoi tessellation with two different depth-to-width aspect ratios (1:10 and 1:100) while maintaining the same channel width of  $3\text{ }\mu\text{m}$ .

Fabrication procedures are described briefly here. Micro- and nanochannels of the nanofluidic chip were formed in double side polished silicon wafers (thickness  $\sim 500\text{ }\mu\text{m}$ ) with two-step reactive ion etching. The positive tone photoresist S1818 was used as the etch mask with the adhesion promoter P-20 for both reactive ion etching steps. First, nanochannels with different dimensions were defined by shallow reactive ion etching, in which plasma was generated by the flow of  $\text{C}_4\text{H}_8$  (60 sccm),  $\text{SF}_6$  (25 sccm), and Ar (2 sccm), with ICP and RF powers of 1200W and 30W, respectively. Etching depth was accurately controlled by etching time based on the etching rate of silicon ( $160\text{ nm/min}$ ). Less than 5 nm variance was observed for the silicon etching of up to depths of 500 nm. Next, two microchannels were defined on both sides of nanochannels using Bosch deep reactive ion etching procedure. Each loop had separate etching ( $\text{SF}_6$  120 sccm for 5 sec) and deposition ( $\text{C}_4\text{F}_8$  140 sccm for 6 sec) steps. The microchannels had cross- section dimensions of  $10\text{ }\mu\text{m} \times 10\text{ }\mu\text{m}$ . Finally, the inlet and outlet holes were formed at the four ends of the two microchannels by a front side Bosch deep reactive etching through the wafer. Thicker photoresist SPR220 7.0 was used as the etch mask for Bosch deep reactive ion etching. The observed selectivity between the etch mask and silicon was  $\sim 0.013$ . Around 5 nm

thick oxide was deposited by atomic layer deposition method onto a chip (of 40mm × 24mm × 0.5mm) to provide a uniform surface energy across the entire channel perimeter. The micro- and nanochannel side of each chip was anodically bonded (330 °C, 1 kV, 1 hr) to a Pyrex coverslip (Pyrex 7740). Before bonding, both silicon and Pyrex substrate were cleaned in Piranha Solution (H<sub>2</sub>SO<sub>4</sub>:H<sub>2</sub>O<sub>2</sub> = 4:1) for 15 min.

These chips are currently being fit with Nanoport Assemblies (N-124S, Upchurch Scientific) by thermally curable epoxy. Assembled chips will be used to conduct single-phase and multi-phase flow experiments in the third year of the project.

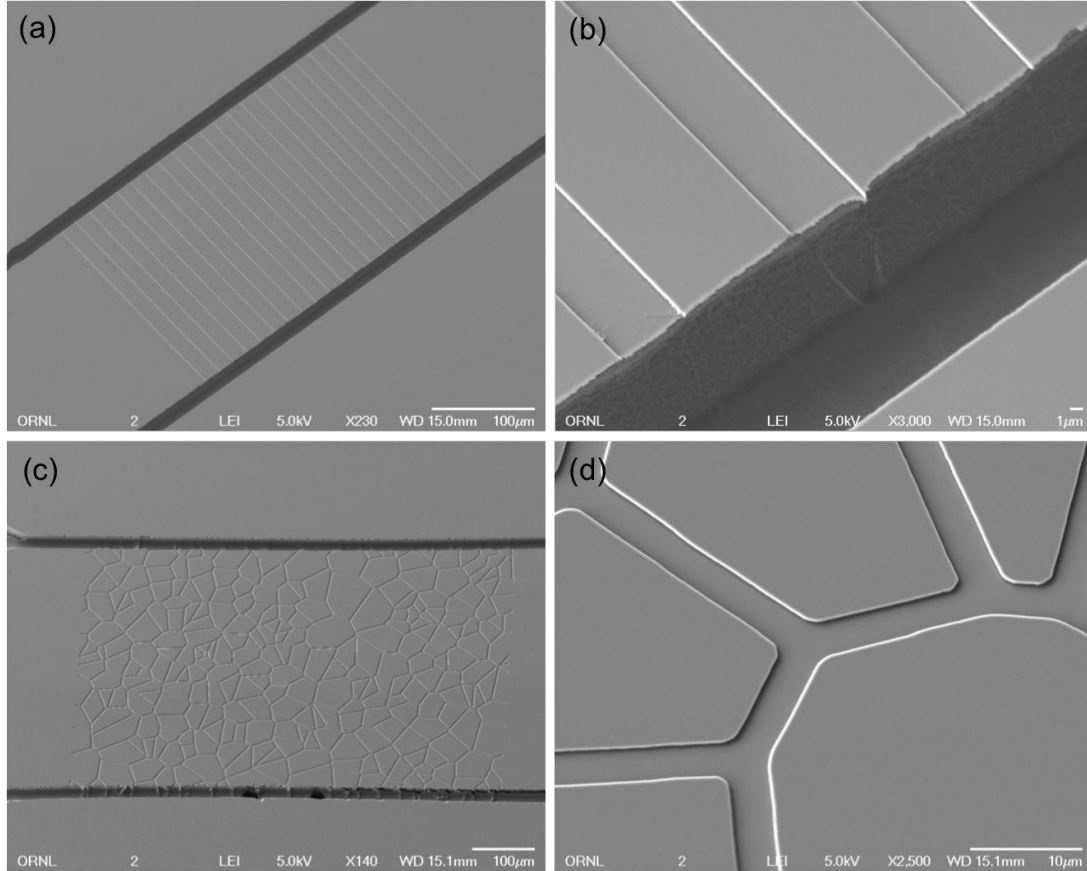


**Figure 1-1: Electron micrographs of silicon parts after forming micro- and nanochannels by two-steps of reactive ion etching.**

(a) - (b) 21 rectangular nanochannel array with 5 μm width, 100 nm depth, and 200 μm length. The distance between adjacent channels is 10 μm. (c) - (d) nanoscale random porous media analog based on Voronoi tessellation; ~300 grains in 400 × 600 μm<sup>2</sup>, 19% porosity, 3 μm width, and 300 nm depth.

## 1.2 Microfluidic Experiments on Water-Oil Multiphase Flows

Nanofluidic chips allow us to conduct experiments on a length scale that is directly relevant to the size of the nanopores. Microfluidic experiments, on the other hand, can help us establish multiphase flow characteristics on the micrometer level without nanoscale effects. These “conventional” data, when compared to the “unconventional”

data obtained from the nanofluidic chips, can help us understand the difference made by the length scale.

We conducted a large set of water flooding and surfactant flooding experiments in poly-dimethylsiloxane (PDMS) microfluidic porous media analogs. These analogs have identical porosity (19%) and the permeability is from 130 to 220 md (Table 1-1). The analogs feature 11 types of geometries, as shown in Figure 1-2.

Table 1-1: Permeability of the microfluidic chips.

Chip Name	U	D	V	H	HV	S	SV	Dia	DiaV	T	TV
$k$ (md)	190	170	150	190	185	215	161	270	190	220	150
Sim. (md)	202	192	220	231	149	237	162	237	152	234	208

Note: The first row is experimental data and the second row is from simulation. The chip names (U-TV) follow the caption of Figure 1-2. U: Uniform channel size; D: Channel size distribution; V: Vugs; H: Hexagons; HV: Hexagons with vugs; S: Squares; SV: Squares with vugs; Dia: Diamonds; DiaV: Diamonds with vugs; T: Triangles; TV: Triangles with vugs.

With these geometries, we tested the effect of the following geometric features on the efficiency of water-oil displacement:

- Coordination number
- Pore (channel) size distribution
- Vugs

The microfluidic models are all hydrophobic (water-PDMS-oil contact angle = 120°) and thus the water flooding experiment is a simulation of the drainage process. The fluids used in these experiments are listed in Table 1-2.

Water flooding tests and surfactant flooding tests were conducted with a constant 5 psia pressure differential between the inlet and the outlet. The resultant capillary numbers, calculated based on the average speed of the front between the start and the breakthrough, were about 2~4 ( $\times 10^{-6}$ ) for water flooding, and 5~8 ( $\times 10^{-5}$ ) for surfactant flooding. At the beginning of the experiments, the chips were saturated with water (with 1.5% wt. NaCl). Then, oil was injected to displace water away from the porous media models. After the irreducible water saturations were established, water (with and without surfactant) was injected again to displace oil to simulate water flooding and surfactant flooding. Displacement efficiency was evaluated using the fraction of oil produced from the models.



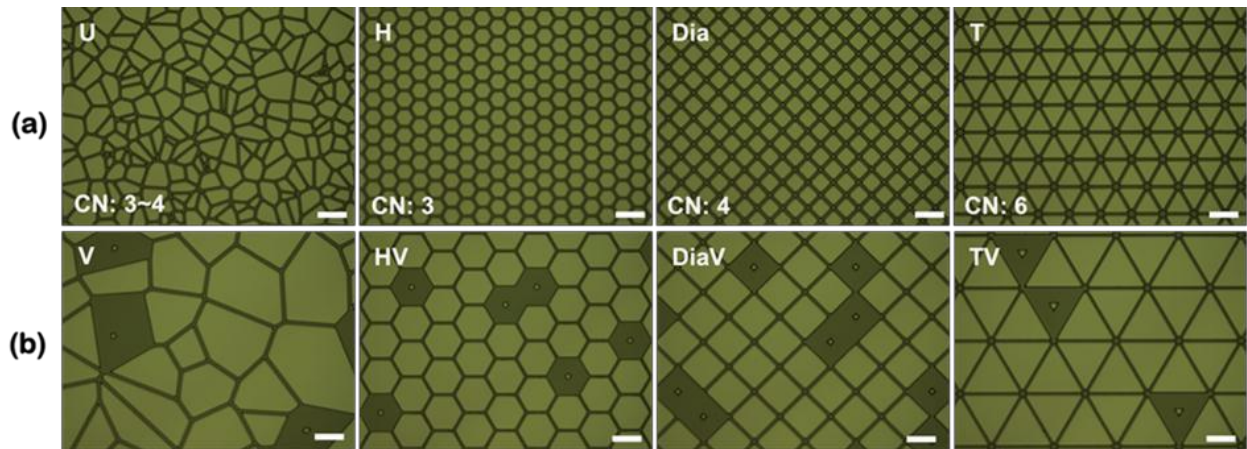


Figure 1-2: Eight of the eleven pore geometries studied for water flooding and surfactant flooding are presented here.

The first row (a) does not contain large pores (vugs). U: randomly connected channels of uniform width (6μm); H: channels (6μm) arranged in hexagonal patterns; Dia: channels (6μm) arranged in diamond patterns; T: channels (6μm) arranged in triangular patterns. The second row (b) contains large vugs. UT: randomly connected channels (8μm) with vugs; HV, DiaV, TV: channels (6μm) arranged in hexagonal, diamond, and triangular patterns with vugs. The three patterns not included in this figure are: square (S), square with vugs (SV), and randomly connected channels with a Gaussian channel size distribution (D: 4-8 μm). CN stands for the coordination number of the geometries.

Table 1-2: Fluids used in the drainage experiments and their properties.

Fluids	Density g/cc	Viscosity cP	IFT dynes/cm
DI water	1	0.89	Not Measured
Brine with Food dye (NaCl:1.5 wt%, Food dye: 1.0 wt%)	1.006	0.94	28.37
Brine with Food dye and EA (NaCl:1.5 wt%, Food dye:1.0 wt%, EA:0.5 wt%)	1.007	1.13	3.57
Mineral Oil	0.848	42.46	N/A

Figure 1-3 shows that the presence of pore (channel) size distribution and the presence of vugs both reduces the displacement efficiency (D vs. U and V vs. U), in agreement with the common notion that pore-scale heterogeneity would reduce the displacement efficiency. Surfactant flooding, in all cases, had increased the recovery of oil by reducing the interfacial tension. This is exemplified in Figure 1-4. The effect of surfactant in vuggy geometries, however, is not as significant as in non-vuggy geometries. Finally, among the eleven geometries tested, it appears that the increase in the coordination number leads to a decrease in the recovery (Figure 1-5).

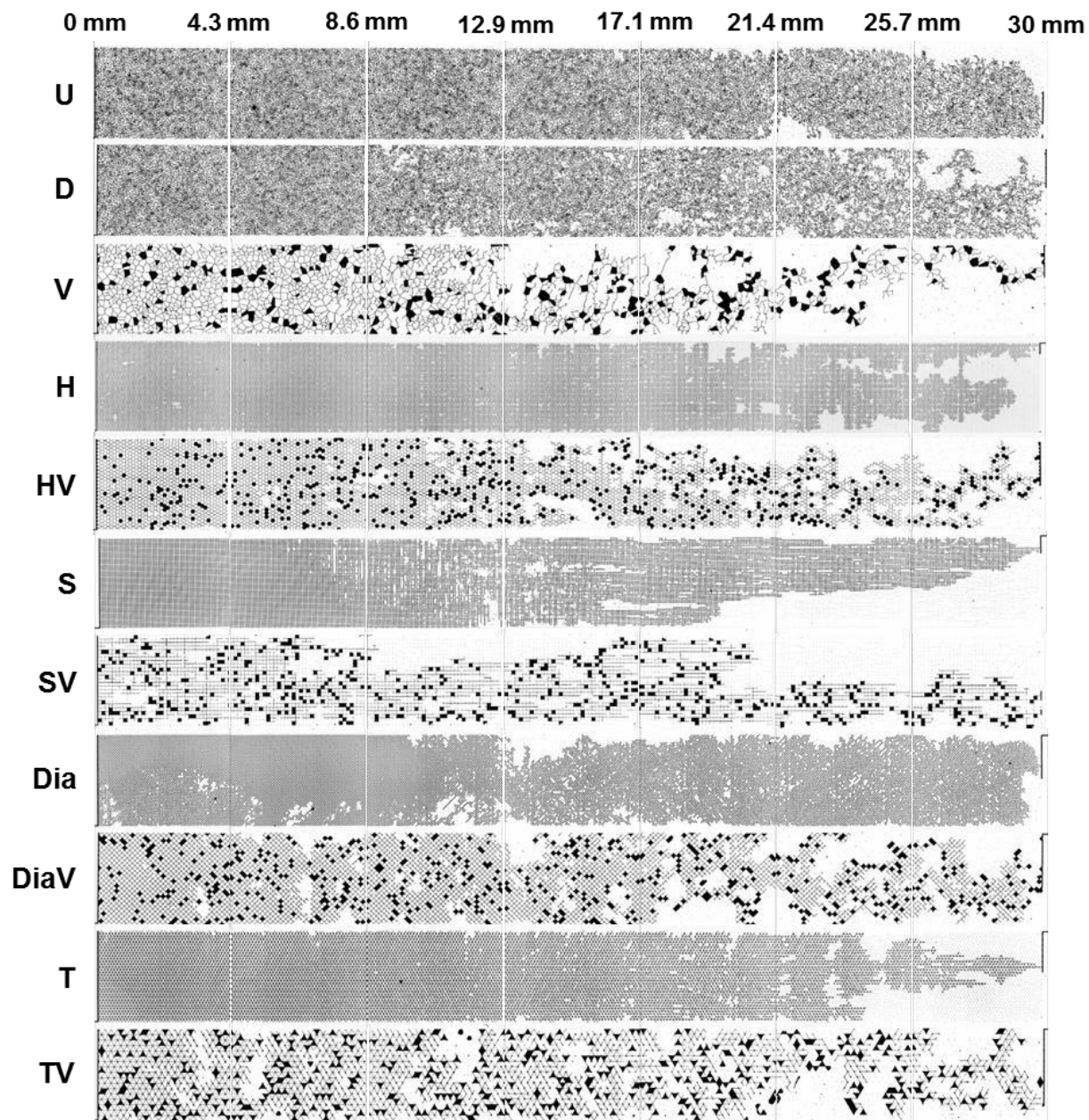


Figure 1-3: Water flooding coverage at the points of breakthrough.



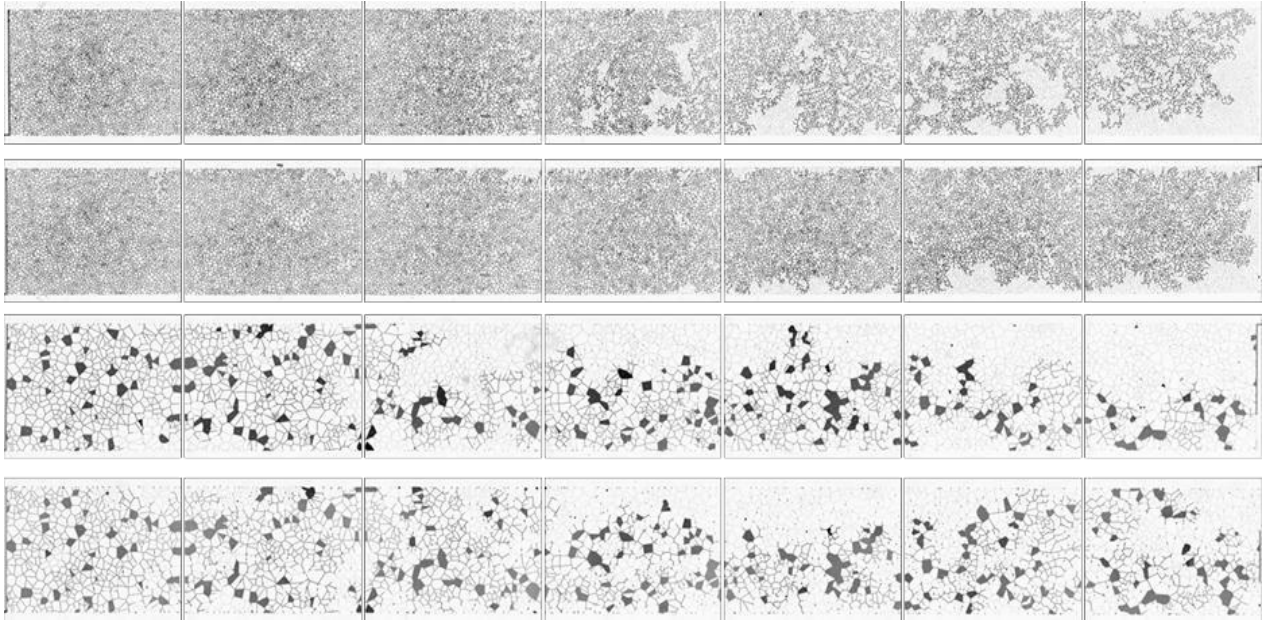


Figure 1-4: Displacement efficiency in chip D (water flooding – first row; surfactant flooding – second row) and in chip V (water flooding – third row; surfactant flooding – fourth row).

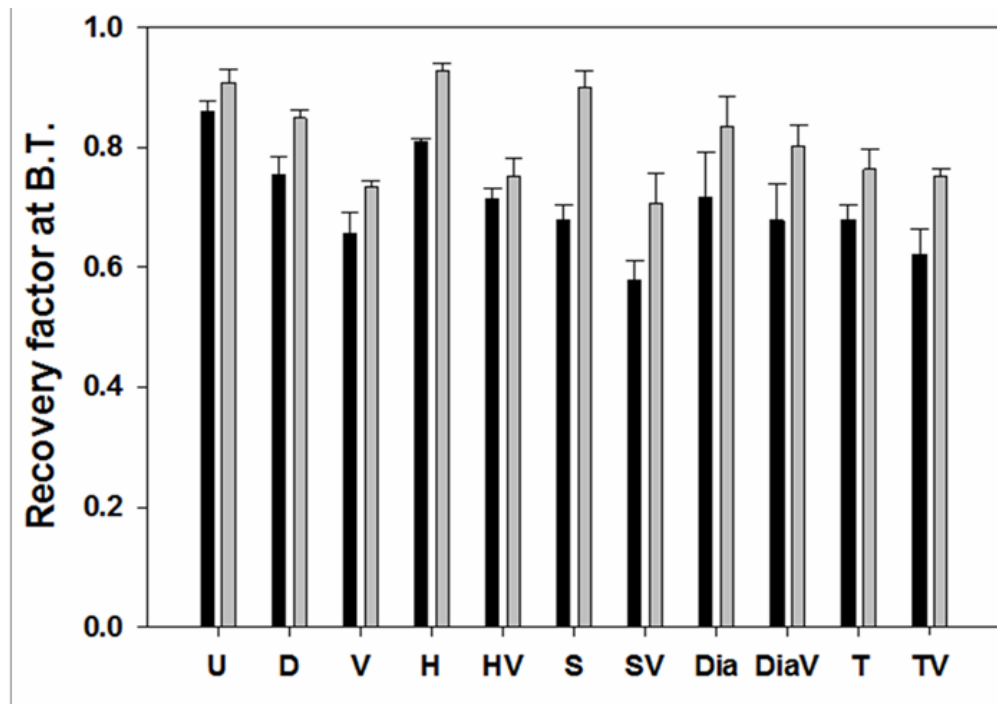


Figure 1-5: Recovery factor at of chips U~TV at points of break-through.

Surfactant (gray bars) has clearly improved recovery over water flood (black bars) in all cases.

### **1.3 Conclusions and Future Work**

The objective of this work is to develop microfluidic and nanofluidic porous media analogs to perform multiphase flow testing on the micrometer and nanometer level, respectively. To this end, we have successfully demonstrated that the feasibility of the approach, the benefit of direct observations, the ability to control porous media properties and to make quantitative measurements on fluid saturations.

## **2. Nano-fluidic chip experiments to understand fluid flow in nano-scale pore spaces and cracks**

### **Part I. Development of optic imaging method for single and two-phase pressure driven flows in nanochannels**

#### **2.1 Introduction**

Over the past decade, the field of microfluidics and nanofluidics has attracted significant research effort with the rapid development of micro/nano-devices fabrication technologies and fluid manipulation systems. Lab-on-a-Chip devices (LOC) and related research have wide range applications and availabilities in fields of biomedical [2, 3], chemical synthesis [4], chemical engineering [5], and petroleum refinery [6]. The understanding of fluid flow behavior is crucial for fundamental study, as well as new technique development and applications.

Three types of actuation principles are commonly applied in microfluidic devices: capillary pumping, mechanical pumping, and non-mechanical pumping, such as electro-osmotic flow (EOF). Among these methods, pressure driven by using a mechanical pump is more often used to study the fluid flow behavior in petroleum engineering.

Pressure driven flow in millimeter and micrometer channels has been well studied and different models have been developed [7-12]. Serizawa et al. [13] carried out visualized investigations on air-water two-phase flow in circular tubes with 20, 25, and 100  $\mu\text{m}$  of inner diameter (i.d.) and steam-water flow in a 50  $\mu\text{m}$  i.d. circular tube, with the velocities covering a range  $J_L = 0.003\text{--}17.52$  m/s and  $J_G = 0.0012\text{--}295.3$  m/s. Some distinctive flow patterns were identified in both air-water and steam-water systems. It has been demonstrated that two-phase flow patterns are sensitive to the surface conditions of the inner wall of the test tube. The comparison of the two-phase flow pattern map with the Mandhane's correlation showed that general trends in microchannels follow the Mandhane's prediction [14]. As the channel dimension decreases, it was found that the properties of fluid flow in sub-micron and nanochannels are not only related to the local shear rate but also dependent on the channel dimensions [10, 15-17]. Travis et al. [15] reported that the classical Navier-Stokes behavior was approached for the channel width of about 10 folds the molecular diameters.

When the dimensions of channels decrease to nano-scale, there are limited studies of single and two phase pressure driven flow due to some major technical challenges. First, the traditional mechanical pumping method is hard to apply to nanofluidic experiments due to the large hydrodynamic resistance and the ultra-small volume of nanochannels. It is very challenging to retain stable pressure and flow rate through the nanochannels by direct pumping. Therefore, an indirect

injection method has been developed and used [10, 18]. The other challenge for the nanofluidic study is the measurement of fluid velocity/flow rate. The optic imaging method is commonly used for single and multi-phase flow rate measurements, since the images can provide real time velocities/flow rates and other important information, such as flow profile, residual layer thickness, and so on. To overcome the lack of sensitivity under small scales, most optic imaging methods use fluorescent tracers, either fluorescent particles or fluorescent molecules [19-21]. Compared to particle imaging velocimetry (PIV), the molecules based method – molecular tagging velocimetry (MTV) [10] is much less intrusive and more suitable for the ultra-small scales of nanochannels due to the much smaller size of molecules compared to particles. Generally the displacement of the tagged region is measured and the velocity profile is determined. Cuenca et al. [10, 18] developed an approach to determine the velocity by measuring the displacement of a fluorescence photo-bleaching line, which is relatively good below the micron scale. For those methods, a complex optical system has to be constructed and aligned in order to perform accurate measurement.

In this study, a novel and comprehensive lab-on-a-chip approach was developed to investigate single/two-phase flow behavior in nanochannels. A concentration dependent fluorescence signal change correlation method has been developed for flow rate determination in LOC devices. The single and two phase flow behaviors in nanochannels were investigated by using these nanofluidic chips. The single phase flow rate versus the pressure drop across the nanochannels was first investigated, and the velocity and channel geometry effects on the two-phase flow patterns were then evaluated. The flow patterns and flow regime map in nanochannels were reported.

## **2.2 Experimental methods**

### **2.2.1 Materials**

High purity nitrogen gas was used as the gas phase. Ultra-pure water was served as the liquid phase and it was pre-filtered with a 0.22  $\mu\text{m}$  pore size Nylon filter before using. Alexa488 (100 mg/L) was purchased from Microprobe and used as the fluorescent dye in the liquid phase.

### **2.2.2 Micro-/Nano-model preparation**

The schematic of nanofluidic chip is shown in Figure 2-1. In order to control the pressure difference across the nanochannels, two microchannels for fluid injection were connected to the nanochannels. The lengths of the microchannels are equal in order to balance the pressure drops. T-shaped junctions were used to connect nanochannels with microchannels to avoid direct injection which may increase the

chance of nanochannel clogging. A total of 100 parallel nanochannels were built between the microchannels to reduce the large hydrodynamic resistance. In order to maintain clean surface conditions, the whole nanofluidic chip was rinsed by lab reagent water, methanol and dried by nitrogen gas prior to use.

### 2.2.3 Experimental setup

Pressure-driven flow was established in the nanochannels by controlling the pressure difference between the two microchannels using the method developed in previous publications [10, 18]. The experimental setup, including the pressure control system, is shown in Figure 2-1. For the single phase flow, pressures  $P_1$  and  $P_2$  were controlled and applied to microchannels 1 and 2 by pressure regulators. Since the hydrodynamic resistance in the nanochannels is much higher than that in the microchannels, most of the injected fluids went through the microchannels. Thus, the contribution of flow in the nanochannels compared to that in the microchannels is negligible and a stable pressure gradient and flow rate can be achieved in the microchannels. For a single nanochannel  $i$ , if its end pressures are named as  $P_{i1}$  and  $P_{i2}$ , the distance from the inlet to this nanochannel is  $L_i$  and the total length of each microchannel is  $L$ , the pressure drop  $\Delta p_i$  will be equal to  $\Delta p_i = \frac{(p_1 - p_2)(L - L_i)}{L}$ . Since the space of nanochannels array is very small ( $< 1$

mm) compared to the length of the microchannel (45 mm), and the nanochannel array connects to the center of the microchannel, the pressure difference across the nanochannels is nearly identical. Since  $L_i \approx \frac{1}{2} L$ , the pressure drop across the

nanochannel array can be defined as:  $\Delta p_i = \frac{p_1 - p_2}{2}$ .

For the two phase flow in nanochannels, there are no well-developed methods for the pressure control and velocity measurement. Therefore, the velocities of two phases were measured indirectly, by controlling the pressures in the two microchannels which, in turn, determine the pressure drop across the nanochannels. Gas and liquid phase were premixed and inlet pressure of the mixer was controlled by the pressure regulator. The average liquid flow rate was determined by the method used for single phase flow, which will be introduced in the results and discussion section. The flow rate of gas phase was determined by measuring the size of the formed gas bubbles in microchannel 2, which served as batch collector. Then the average velocities of gas and liquid phases in the nanochannels were calculated based on the flow rate divided by the volume of the nanochannel.

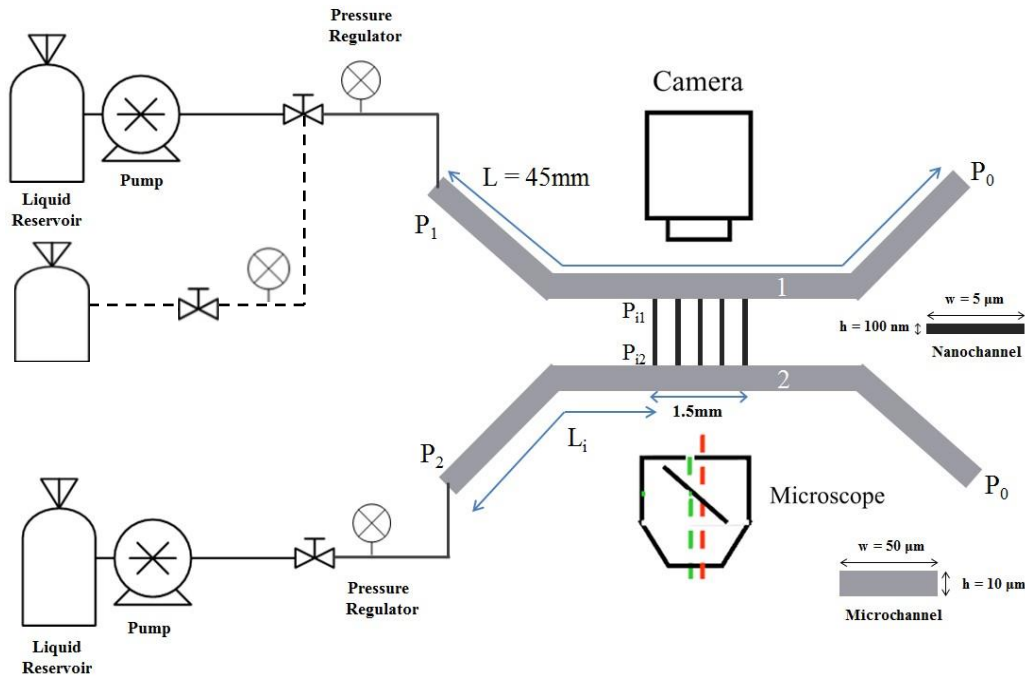


Figure 2-1: Fluid transport system and schematic of the nanofluidic chip.

Solid lines are for liquid transportation and the dotted line is for gas transportation in two-phase flow experiments.  $P_1$  is inlet pressure on microchannel 1,  $P_2$  is inlet pressure on microchannel 2;  $P_0$  is outlet pressure for both microchannels;  $P_{i1}$  and  $P_{i2}$  are the end pressures of the selected nanochannel;  $L$  is the total length of each microchannel,  $L_i$  is the distance from the microchannel inlet to connection of the selected nanochannel.

## 2.3 Results and discussion

### 2.3.1 Flow rate determination and single phase flow in nanochannels

Unlike two phase flow, no interface can be used to monitor flow rate for single-phase flow. Thus, it is not possible to determine flow rate by tracking the interface. As discussed in the Introduction,  $\mu$ PIV (particle imaging velocimetry) is also not viable due to the small size of the channels. MTV (molecular tagging velocimetry) and newly developed photo-bleaching velocimetry [18, 19] are commonly considered to be suitable for the velocity measurement in nanochannels. However, there are still some limitations such as poor imaging signals and complex optic arrangement. Thus, we developed a novel method to determine the flow rate in nanochannels by measuring the concentration dependent fluorescence signal change based on the Beer Lambert's law. The principle of Beer Lambert's law has been widely used in the spectroscopic photo-detector such as UV/Vis detector to measure the concentration of organic compounds. Based on Beer Lambert's law, the fluorescence concentration detector has been developed and used in microfluidic devices [22]. The equation of Beer Lambert's law is given as:



$$\varepsilon l c = \ln \frac{P_0}{P_T} \quad (2.1)$$

Where  $P_0$  is the intensity/power of the incident light,  $P_T$  is the intensity/power of the transmitted light,  $l$  is the length of light path,  $c$  is the concentration of the fluorescence dye and  $\varepsilon$  is the molar absorption coefficient under wavelength  $\lambda$ . The absorbed light intensity,  $P_A$ , could be expressed as:

$$P_A = P_0 - P_T = P_0(1 - e^{-\varepsilon l c}) \quad (2.2)$$

The emitted fluorescence light power ( $P_F$ ) will be proportional to absorbed light intensity and quantum yield of fluorescence dye ( $\phi$ ):

$$P_F \propto \phi \cdot P_A \propto \phi \cdot P_0(1 - e^{-\varepsilon l c}) \quad (2.3)$$

By simplifying the equation:

$$P_F = k'(1 - e^{-\varepsilon l c}) \quad (2.4)$$

Where  $k'$  is a lumped parameter that depends on input power, quantum yield of the fluorescence dye and the collection efficiency of the optic system.

Since the intensity of the emitted light is measured by an optical detector (camera), the responses of the camera and the background signals also need to be taken into consideration. The response of the ICCD camera is generally determined by the photocathode material used in the Image Intensifier and it is wavelength dependent. Since the same fluorescence dye is used, the responsiveness is considered to be a fixed number. The background signal is defined as the signal without addition of fluorescence dye, which is generally caused by the dark current of the optic detector or the light leaking in the optical system [22]. Both of them are related to the input power of the excitation light. In order to reduce the effect of background noise, input power is set to a fixed number and the background intensity is measured as  $I_B$ . Thus, the normalized signal intensity in the optical detector which contributed by the emitted light is calculated as:

$$I_{(c)} = I_S - I_B \quad (2.5)$$

Where  $I_{(c)}$  is the normalized signal intensity contributed from the emitted fluorescence light,  $I_S$  is the collected signal intensity, and  $I_B$  is the measured background intensity.

The normalized fluorescence signal as a function of dye concentration ranging from

$10^{-9}$  mole/L to  $10^{-5}$  mole/L was measured and the results are shown in Figure 2-2. The molar concentrations of fluorescence dye are on the X-axis and the intensity of fluorescence signals (signal-background)/background are on the Y-axis. Figure 2-2(a) shows the entire tested fluorescence concentration range and Figure 2-2(b) shows the enlarged part of the Figure 2-2(a) where the concentrations of fluorescence dye is in the range from  $10^{-8}$  mole/L to  $10^{-6}$  mole/L. It was found that experimental results fit very well into theoretical calculations in the concentration range from  $10^{-8}$  mole/L to  $10^{-6}$  mole/L. Deviation is observed when the concentration is above  $10^{-6}$  mole/L, which indicates the decrease of quantum yield caused by aggregation of dye molecules or a self-quenching effect [23, 24]. Thus, the concentration of fluorescence dye we used was below  $10^{-6}$  mole/L to guarantee the accuracy of the method.

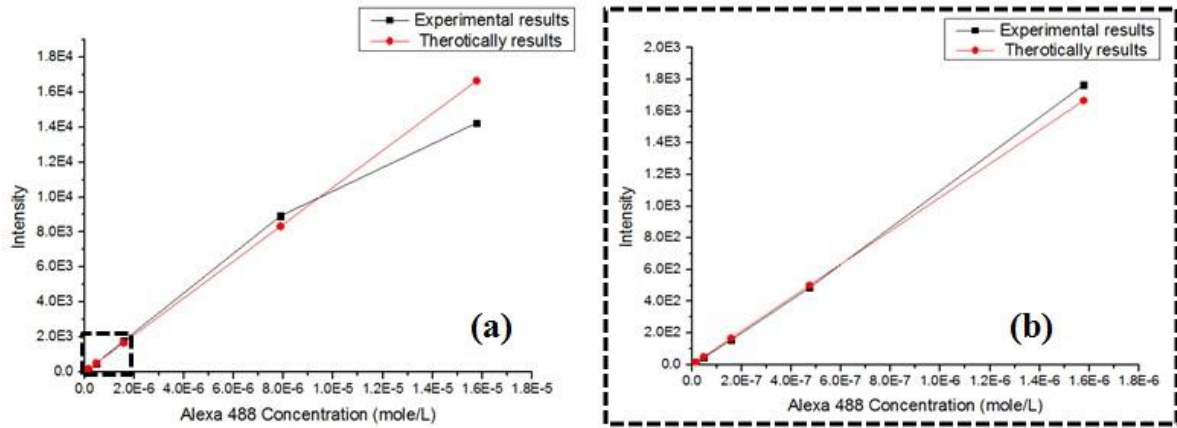


Figure 2-2: Comparisons between experimental results and theoretical results of intensity changes with different fluorescence dye concentration.

(a) Entire range of fluorescence signal intensity change vs. fluorescence dye concentrations; (b) Enlarged figure of fluorescence signal intensity change vs. fluorescence dye concentrations at a low concentration range ( $10^{-8}$  mole/L to  $10^{-6}$  mole/L).

Referring to Figure 2-1, stable pressure driven flow was established and microchannel 1 served as the inlet channel. Microchannel 2 served as the outlet and batch collector. One end of microchannel 2 was connected to a small capped vial. The concentration of fluorescence dye was maintained at  $C_1$  in microchannel 1 while the initial concentration of dye in microchannel 2 was  $C_2$  ( $C_1 \gg C_2$ ). As the solution in microchannel 1 flowed into microchannel 2 through the nanochannels, the concentration of dye in microchannel 2 would gradually increase to  $C_2'$  after certain time,  $t$ . Therefore, the average volume flow rate in each single nanochannel could be obtained from:

$$\bar{q} = \frac{V(C_2' - C_2)}{nt(C_1 - C_2')} \quad (2.6)$$

Where  $V$  is the volume of the microchannel,  $n$  is the total number of nanochannels,  $t$

is the time window between two measurements. Because the volume of the microchannel is much larger than the volume of nanochannels, all measurements were taken at least five minutes after the pressure was stable to ensure that the fluorescence signal in the microchannel 2 had a significant change. Since this method is based on the mass transportation of the fluorescence molecules, the effects of diffusion need to be considered. The diffusion coefficient of the fluorescence dye, Alexa 488, in aqueous solution, is  $430 \mu\text{m}^2/\text{s}$  at room temperature ( $25^\circ\text{C}$ ) [40]. For a given residence time, the average diffusion distance of the fluorescence dye is:

$$d = \sqrt{D \cdot t} \quad (2.7)$$

Where  $D$  is the diffusion coefficient of the molecule,  $t$  is the residence time. Under the experimental conditions, the residence time of the fluorescence dye in the nanochannels is very small (0.1-0.3 s). The average diffusion distance is calculated to be less than  $10 \mu\text{m}$ , which is much smaller in comparison to the length of a nanochannel ( $200 \mu\text{m}$ ). Therefore, the contribution of the diffusion to mass transportation can be neglected.

By using this method, the rate of single phase pressure driven flow through  $100 \text{ nm}$  depth nanochannels under different pressures was measured and data is compared with theoretical results obtained from Poiseuille's Law. The theoretical volumetric flow rate varies linearly with pressure, which is integrated from Hagen-Poiseuille's equation [25]. The average volumetric flow rate ( $q_n$ ) in the nanochannel is given by:

$$q_n = \frac{\Delta p \cdot h^3 w}{12l \cdot \eta} \quad (2.8)$$

Where  $\Delta p$ ,  $h$ ,  $w$ ,  $l$ , and  $\eta$  correspond to pressure drop, height of cross section, width of cross section, length of the nanochannel and viscosity of the fluid, respectively.

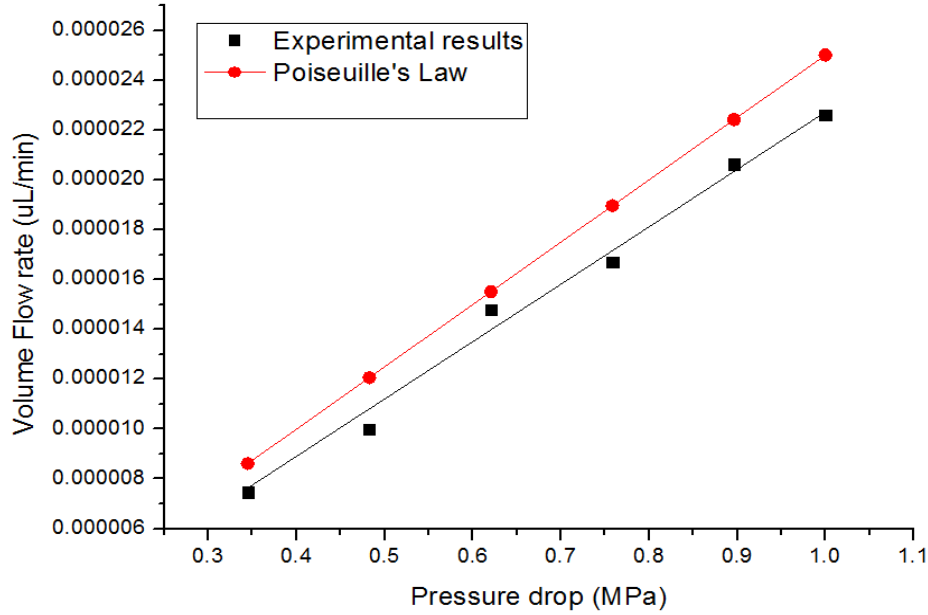


Figure 2-3: Average volumetric flow rate vs. pressure drop in a nanochannel.

The red dots and curve in Figure 2-3 shows the theoretical line based on the integrated Hagen–Poiseuille’s equation, where a  $1.0 \times 10^{-3} \text{ Ns/m}^2$  water viscosity was used since the experiments were conducted at a  $20^\circ \text{C}$ . The black dots and curve show the experimental results. The experimental average volumetric flow rate was slightly lower than theoretical results. This phenomena is also reported in other publications [10, 17, 26], which they suggested that the property of solution, such as apparent viscosity, may change depending on the size of the channels. Another possible reason may be due to partial collapse of the channel cross sections. Since the aspect ratio of nanochannel is relatively big ( $w/h = 50$ ), a small amount of buckling of the pyrex glass may have occurred while the pyrex and silicon wafers were being anodically bonded [18]. Thus, the effective area of the nanochannel cross section may be smaller than the calculated number, which will lead to the slower flow rate.

### 2.3.2 Two phase flow regime map in the nanochannels

In this section, experiments of nitrogen/water two phase flow in nanochannels were conducted and flow profile images are shown in Figure 2-4. Three types of flow profiles were observed in the nanochannels under experimental conditions. Some of them were also reported in millimeter and micrometer sized channels in previous publications [27, 28].

Based on the flow profile and velocities, a flow regime map was generated from a total of 49 experiments and is shown in Figure 2-5. The observed flow regimes corresponded to these ranges of gas and liquid velocities are: gas velocity ( $J_G$ )  $0.005 \sim 0.02 \text{ m/s}$  and liquid velocity ( $J_L$ )  $1.0\text{E}^{-5} \sim 9.4\text{E}^{-4} \text{ m/s}$ , respectively.

Annular flow was observed when the gas velocity was relatively high ( $>0.0116$  m/s) within the whole liquid velocity range. A continuous gas core occupied most of the channel while a liquid “film” with a thickness ranging from 0.9 to 1.6  $\mu\text{m}$  formed at the side walls. Note that the thinnest dimension of the “film” was still in the direction perpendicular to the observer (100 nm), thus the “film” was in zones near the sides of the channel that are not swept by the gas. It was noticed that the thickness of liquid films decreased with increasing gas velocity. The hydrophilic inner wall determined the formation of liquid films. When the gas velocity was high enough, gas will penetrate through the liquid phase to form a gas core and the flow pattern will change from segmented flow to annular flow.

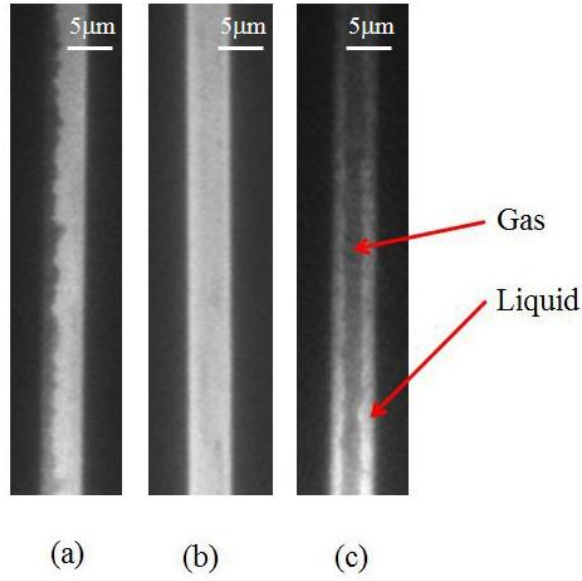


Figure 2-4: Water/gas two phase flow patterns in nanochannels.

The Dark region in the channel is gas phase while the bright region in the channel is water. (a) stratified flow; (b) single phase flow; (c) annular flow.

The stratified (wavy) flow pattern was found when both gas and liquid phases had relatively low velocities (gas velocity ( $J_G$ ) < 0.0068 m/s and liquid velocity ( $J_L$ ) < 0.00027 m/s). The interface between gas and liquid was not flat/smooth. At relatively low gas velocity ( $J_G$  < 0.0094 m/s) and a relatively high liquid velocity ( $J_L$  > 0.00031 m/s), an interesting pattern was observed - single phase flow pattern. Liquid occupied the entire cross-section while the gas phase was not found in the nanochannels. Overall slug flow and dispersed bubbly flow were not observed. Those two patterns are commonly observed when flow channels are in the millimeter and micrometer size ranges and in the case when liquid velocity is much higher than gas velocity. For slug flow, the gas slugs occupy most of the channel cross-section and are separated by the liquid plugs. When the liquid velocity increases, gas slugs and bubbles are deformed and scattered in the continuous liquid phase. The reasons that slug flow and bubbly flow were not observed in the nano-channels were due to geometry features, the small dimensions and the relatively high aspect ratio of the channel cross section ( $w/h = 50$ ). When confined to small dimensions, the rigidity of gas bubble is relatively high and gas bubbles will maintain the spherical shape to reduce surface tension. Thus, the cross-section of each nanochannel in our experiments is too wide for a gas bubble to occupy the entire cross-section. Also, at low injection pressure, since the inner wall of the nano-channels appeared to be hydrophilic, the liquid phase (water) can be spontaneously imbibed into the nanochannels whereas any gas motion must overcome the capillary forces. The nanochannels were liquid filled because the driving pressure was too low for the gas phase to enter the nanochannels.

It is noticed that both gas and liquid velocities were ultra-small in the experiments comparing to the flow regime results in conventional-sized channels which had sub-mm and mm inner diameters. Typically only one flow pattern is presented at such low velocities in conventional-sized channels and mostly is segmented flow (bubbly or slug). Serizawa et al. [13] reported that bubbly flow pattern observed while the  $J_G$  ranging from 0.001 to 0.5 m/s and  $J_L$  ranging from  $1.0^{-4}$  to 0.1 m/s, which covers the experimental conditions in this work. However, the dimensions of channels in this work is much smaller ( $5\ \mu\text{m} \times 100\ \text{nm}$ ) and the flow regimes were much more sensitive to the velocity difference between water and gas, in which three different flow patterns were observed. By comparing the flow regime maps between presented results and conventional-sized pipes, the presence of annular flow and stratified flow had partial agreement with the flow regime in larger channels [29-31], while bubble flow and slug flow were not observed in this work. Like we mentioned above, the high aspect ratio and small dimension of the channels significantly affect the formation of gas bubble and gas slug [13, 32].

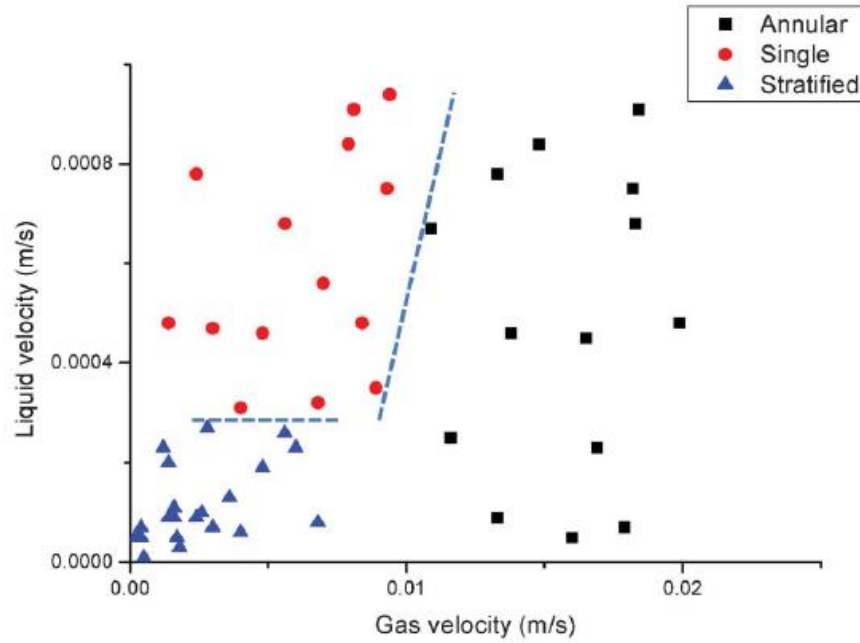


Figure 2-5: Water/gas two phase flow regime map in nanochannels

## 2.4 Conclusions

A novel optical method for single and two phase flow in nanochannels was developed. Pressure drops in the nanochannels were controlled and stable pressure driven flows were achieved. Meanwhile, a concentration dependent fluorescence signal correlation method was developed to measure the volume flow rate in nanochannels. Single liquid phase and gas/liquid two phase pressure driven flows were performed in nanochannels. For the single liquid phase flow, linear correlations between flow rate and pressure drop were obtained which closely fit with theoretical values from Poiseuille's Law. Gas/water two-phase flow were performed in nanochannels and flow patterns were characterized into three different types - single phase flow, stratified flow, and annular flow and their detailed features are described. A two-phase flow regime map was also constructed. It was found that the two-phase flow profiles in nanochannels are essentially different on several points from those of two-phase flows encountered in ordinary scale tubes and channels with mild cross-section aspect ratios. No segmented flow, bubbly flow or gas slug flow, was observed in nanochannels under the conditions where expected at more ordinary scales. The result will provide crucial information for the analysis of multi-phase flow in nanochannels.

## Part II. Gas/fluid flow behavior in the nanochannels

### 2.5 Introduction

Compared with conventional gas reservoirs, shale gas reservoirs have very small pore sizes, in the range of 1 to 300 nanometers. Additionally, the matrix permeabilities of those unconventional gas reservoirs are in the microdarcy ( $\mu\text{D}$ ) to nanodarcy (nD) range. Under such small diameters of the flow channels within the shale rock, it is necessary to consider the effects of the molecular interaction between the fluid and the flow channel walls. These effects can usually be ignored for flow in conventional reservoirs with much larger pore throats. Studying flow mechanisms such as slip flow and diffusive flow [33] become important in order to understand flow in shale gas reservoirs.

Extensive studies have been conducted on single-phase flow in tight sand and shale gas systems, and equations have been derived to measure the relative permeability of gas and to determine the single-phase gas slippage effect [33-35]. Swami and Clarkson [36] summarized and compared several methods for quantifying non-Darcy flow in unconventional gas reservoirs. Jones and Owens [37] conducted permeability measurements on over 100 samples from various tight shale plays and derived empirical relationships between the slippage factor and reference permeability. Javadpour [33, 34] introduced a new term, apparent permeability, to describe the complexity of gas flow in nanochannels, by incorporating both Knudsen diffusion and slippage effect. It was found that the ratio of apparent permeability to



Darcy permeability increases sharply as pore sizes decrease to smaller than 100 nm.

However, under real shale gas reservoir conditions, two phases (mostly water and gas) typically exist. It has been reported that in some ultra-low permeability shale gas reservoirs, water saturation could be much greater than that in conventional shale gas plays. The effects of remaining water saturation on the gas permeability/relative permeability and gas slippage still have not been investigated sufficiently. Several studies have reported that the gas slippage factor for two-phase flow is affected by relative permeability and water saturation [38-43]. Some of these researchers found that the two-phase gas slippage factor tends to decrease as water saturation increases. However, Li and Horne [39] reported contradictory results, finding that the two-phase gas slippage factor increased as water saturation increased. Thus, more research in this area is required.

For laboratory experiments, shale samples were used in most cases in order to represent the real pore structure and distribution in the reservoir. However, there are some limitations of using shale samples in laboratory experiments. For example, water saturation and saturation distribution are difficult to measure. Meanwhile, the lab-on-chip technique is becoming a suitable approach for investigating fluid flow in ultra-small pores. Nanofluidics and microfluidics have been used in different areas for both fundamental research and application. Some micromodels are being used to study multiphase flow under both saturated and unsaturated conditions. Furthermore, the lab-on-chip technique provides a means by which to directly visualize fluid flow behavior, such as the displacement of one fluid by another, because most micro/nanofluidic chips are made of transparent materials. Micromodels have also been used to simulate numerous porous media transport phenomena, including microorganism transport in unsaturated porous media [44], bacteria dispersion in bioremediation strategies [45], and enhanced oil recovery [46-48]. However, visualization studies of fluid flow in nanochannels are still lacking, especially for shale gas and tight gas.

In this work, water/gas two-phase displacements in 100 nm-deep channels were characterized, and the two-phase gas slippage effect was investigated by using the novel optic imaging system developed in the Part I.

## **2.6 Experimental method**

### **2.6.1 Materials**

High purity nitrogen gas was used as the gas phase. Ultra-pure water served as the liquid phase and was pre-filtered by a 0.22  $\mu\text{m}$  pore size Nylon filter before using. Alexa 488 (100 mg/L) was purchased from Microprobe and used as the fluorescent dye in the liquid phase.

Because the primary objective of this study was to investigate the two-phase flow in

nanochannels, the nanochannel array served as the test section. It was considered a porous media consisting of 100 nanochannels. The isolated schematic of the test section is shown in Figure 2-6. The test section was 1500  $\mu\text{m}$  in width and 10  $\mu\text{m}$  in height; the length of the test section was equal to the length of each nanochannel, which was 200  $\mu\text{m}$ . In the experiments, two microchannels were not considered as part of the test section and were used instead to introduce fluids and control the pressure drop.

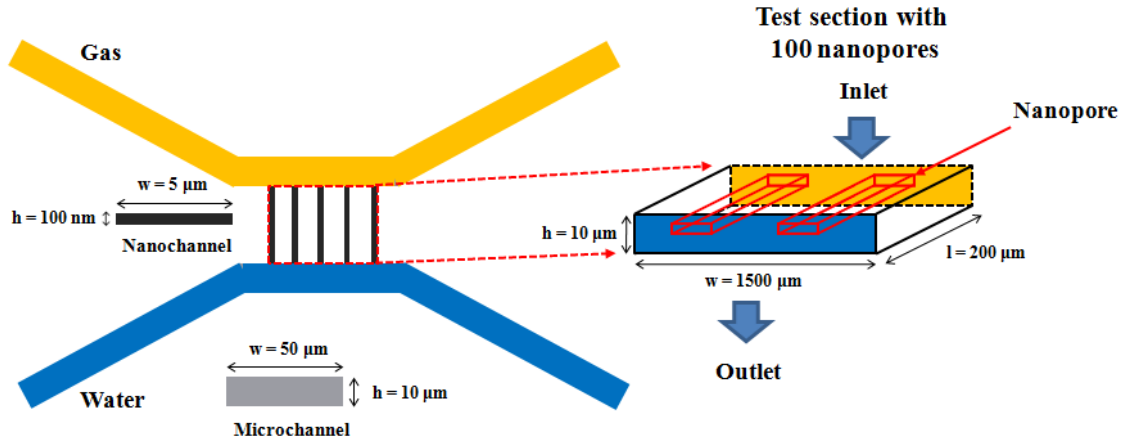


Figure 2-6: Schematic of nanochannel array as the experimental test section

## 2.6.2 Experimental procedure

Before every set of experiments, preliminary tests were conducted with the nanofluidic chip; no leakage was observed, and the flow was stable. The nanochip was cleaned by 0.1 mole/L HCl, methanol and deionized water prior to use. All experiments were conducted at room temperature.

Gas displacing water:

The nanochannels first were 100% saturated with water; then, nitrogen gas was pressure-injected into them to simulate the flow back. In order to calculate the intrinsic gas permeability at different water saturation levels, the apparent gas permeability was measured under different mean pressure  $p_{mi}$  at the same remaining water saturations  $S_{wi}$ . Various remaining water saturations were obtained by applying different pressure drops ( $\Delta p_i$ ) on the test section. The applied mean pressure was always smaller than the pressure drop used to obtain the given remaining water saturation ( $p_{mi} < \Delta p_i$ ) and images were taken by the microscope to ensure that the water/gas ratio did not change after the experiments. The detailed procedure is discussed in the results section.

Water displacing gas:

For the water displacing gas experiments, the nanochannels were saturated with nitrogen gas. The gas phase was displaced by water at a constant pressure drop until a constant gas/water ratio was obtained. The total water flow rates were monitored.

## 2.7 Result and discussion

### 2.7.1 Theory

The gas slippage effect was first studied by Klinkenberg [49] and the Klinkenberg equation is expressed as follows:

$$k_g = k_{g\infty} \left(1 + \frac{4c\lambda}{r}\right) \quad (2.9)$$

Where  $k_g$  is the apparent gas permeability at a mean pressure,  $p_m$ ; where  $p_m = \frac{p_i + p_o}{2}$ ;  $p_i$  and  $p_o$  are inlet and outlet pressure of the test section, respectively.  $k_{g\infty}$  is the intrinsic permeability of gas at infinite pressure,  $\lambda$  is the mean free path of gas molecule,  $r$  is the radius of the pore and  $c$  is a constant.

Klinkenberg deduces the Eq 2.9 to:

$$k_g = k_{g\infty} \left(1 + \frac{b}{p_m}\right) \quad (2.10)$$

Where  $b$  is the gas slip factor, which is defined as:

$$b = \frac{4c\lambda p_m}{r} = \frac{4c'}{r} \quad (2.11)$$

Since the mean free path of the gas is inversely proportional to the mean pressure,  $p_m$ , the factor  $c'$  would be a constant at a certain mean pressure. From Eq. 2.11, the gas slip factor is inversely proportional to the radius of the pore. Li et al [39] claimed that the slip factor increased with decreasing effective pore radius caused by saturated liquid.

According to Darcy's equation, in the gas/water two phase flow, the effective gas phase permeability is calculated as:

$$k_g(S_w, p_m) = \frac{2q_g \mu_g L p_o}{A(p_i^2 - p_o^2)} = \frac{q_g \mu_g L}{A \Delta p} \frac{p_o}{p_m} \quad (2.12)$$

Where  $k_g(S_w, p_m)$  is the effective gas phase permeability at a water saturation of  $S_w$

and a mean pressure of  $p_m$ .  $q_g$  and  $\mu_g$  are the flow rate and viscosity of the gas phase, respectively.  $p_i$  and  $p_o$  are the inlet and outlet pressures and  $p_m$  is the mean pressure.  $A$  and  $L$  are, respectively, the cross sectional area and length of the flow.  $\Delta p$  is the pressure drop between inlet and outlet. With consideration of gas slip effect, the intrinsic effective permeability of the gas phase, which is pressure-independent, is presented with the following equation:

$$k_{g\infty}(S_w) = \frac{k_{g\infty}(S_w, p_m)}{(1 + \frac{b_{S_w}}{p_m})} \quad (2.13)$$

Where  $k_{g\infty}(S_w)$  is the intrinsic permeability of the gas phase and  $b_{S_w}$  is the gas slip factor for a water saturation of  $S_w$ . For the low permeability unconventional shale gas reservoirs, since the gas slip effect may not be neglected, gas relative permeability can be computed by Eq. 2.13.

Based on the experimental conditions and geometry of the test section used in our work, the Knudsen number has been calculated. The Knudsen number is an important factor which predicts the flow regime:

$$K_n = \frac{\lambda}{d} \quad (2.14)$$

Where  $d$  is the pore diameter and  $\lambda$  is the mean free path of the molecules, which is defined as:

$$\lambda = \frac{\mu}{p_m} \sqrt{\frac{\pi RT}{2M}} \quad (2.15)$$

Where  $\mu$  is the viscosity of gas molecules,  $p_m$  is the mean pressure,  $R$  is universal gas constant ( $R=8.314$  J/(mole·K)),  $T$  is the absolute temperature and  $M$  is the gas molecular mass. Based on the Knudsen number, various flow regimes can be identified as shown in Table 2-1 [50].

**Table 2-1: Flow regime based on Knudsen number**

Knudsen number ( $K_n$ ) range	Flow regime
$\leq 0.001$	Viscous flow
$0.001 < K_n < 0.1$	Slip flow
$0.1 < K_n < 10$	Transition flow
$K_n \geq 10$	Knudsen's (free molecular) flow

In our experiments, most flow regimes fall into the slip flow region. In this flow regime, viscous flow theory has to be modified to accommodate the slip boundary conditions. Many tight gas plays fall into this region and Klinkenberg's slippage theory holds well for most of them. Eq. 2.12 is used to determine the apparent gas permeability and the intrinsic gas permeability is calculated.

The flow mechanism is another interest of this study since the optic lab-on-chip method provides us the chance to directly visualize the two phase flow behavior in the nanochannels. It is agreed [51] that there are two major concepts pertaining to immiscible fluid flow in porous media: the channel flow and the funicular flow. For channel flow, each phase moves through its own separate network of interconnecting channels. In this concept, as the water saturation increases, there is an increase in the number of channels filled with water and a corresponding decrease in the number of channels filled with gas. Under these conditions saturation water tends to fill the smaller channels since it is the wetting phase and gas phase tends to occupy the larger pores. Thus the average radius of the gas channels is increasing with the increase of water saturation. From Eq. 2.11, the slip factor is inversely proportional to the average radius of the channel. Therefore, the slip factor may decrease with the increase of water saturation. This phenomenon has been well modeled by the invasion percolation.

In the funicular flow concept, the channel/pore is occupied by both gas and water flow, where water is near the inner wall and gas is on the inside and occupies the central portion of each channel. Under this condition, the thickness of water layer increases with the increase of the saturated water, which will result the decrease of the effective radius of gas channel. Thus, the gas slip factor is increasing.

In real shale/core samples, it is very difficult to obtain accurate water saturation and the distribution of water saturation. As a result, it is almost impossible to determine which type of the flow (channel flow or funicular flow) is governing in the immiscible two phase flow in shale/core samples. In our work, the flow pattern was observed from the real-time imaging data, which will be discussed in the next paragraph.

### **2.7.2 Gas displacing water and two phase gas slippage effect in nanochannels**

Experiments of gas displacing water (flow back) were conducted in nanochannels. The injection pressure of nitrogen gas was ranging from 10 psi to 90 psi. Flow rate and flow profiles of gas displacing water were obtained from microscopic images. Overall, the remaining water saturation obtained from imaging data was below 42%. The remaining water saturations obtained in our experiments are significantly higher than the results from most shale samples and micro-scale models.

The two phase flow patterns of gas displacing water in nanochannels are

demonstrated in Figure 2-7. Three types of flow patterns were observed. In the first case (a) gas flow occupied one side of the channel after breakthrough while water phase was trapped on the other side of the channel. In the second case (b), a gas core was filled the middle of the nanochannels which are surrounded by water layer on the side walls. In the last case, gas phase occupied the majority of the channel where only some discrete water plugs (c) were attached in the channel.

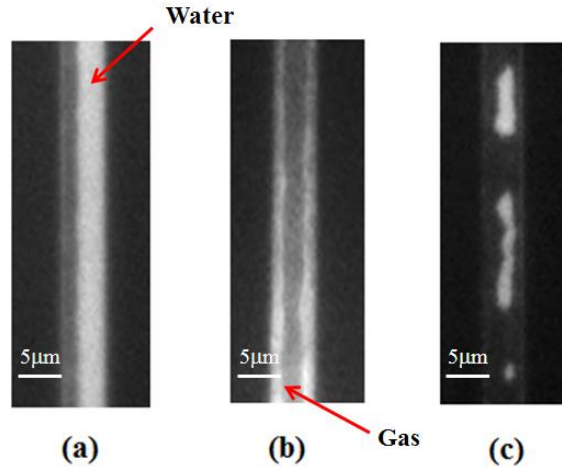


Figure 2-7: Flow patterns of immiscible two phase flow in nanochannel.

The Dark region in the channel is gas phase while the bright region in the channel is water: (a) side flow of gas; (b) annular flow; (c) water slug.

In order to investigate the two phase gas slippage effect, various remaining water saturations were obtained by using the method described below. Figure 2-8 to Figure 2-10 summaries the procedure to achieve water saturation and the image data is also showed. The bright field in Figure 2-8 to Figure 2-10 represents water phase because the addition of fluorescence dye and the dark field in the channel represents the gas phase. In the step 1, shown in Figure 2-8, the test section was first pressure-filled by water from microchannel (2) and the water saturation was around 94%, as measured by imaging process. In the step 2 (Figure 2-9), the gas phase was then injected into the test section via microchannel (1), under a stable pressure of  $p_1$ , which will be denoted as starting pressure. After the water saturation was reduced to a constant ratio, 29.7% in Figure 2-9 for instance; gas permeability measurements under this water saturation were conducted by applying several different pressures,  $p_i$  ( $p_i < p_1$ ). Since  $p_i$  is smaller than  $p_1$ , remaining water saturation was maintained at the same amount during the measurement (Figure 2-10). After a series of gas permeability measurements were made at the same remaining water saturation, another set of experiments was repeated from Step 1. The results are summarized in Figure 2-11.

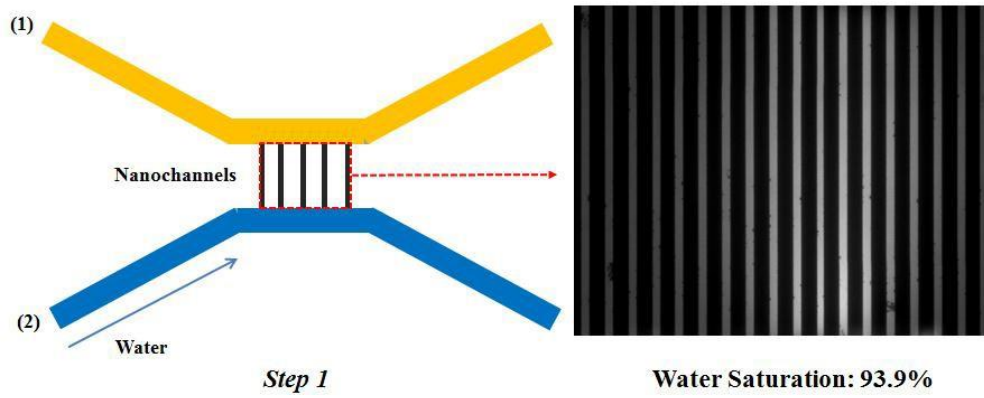


Figure 2-8: Measurement of gas permeability at different water saturation, step 1.

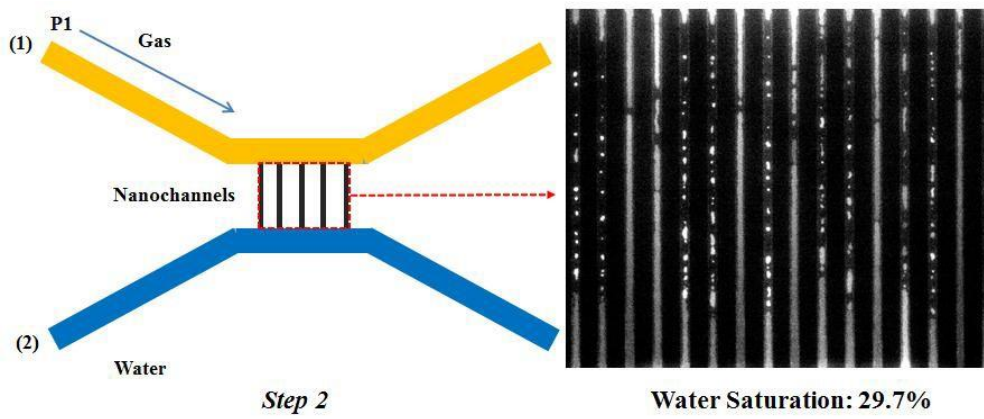


Figure 2-9: Measurement of gas permeability at different water saturation, step 2.

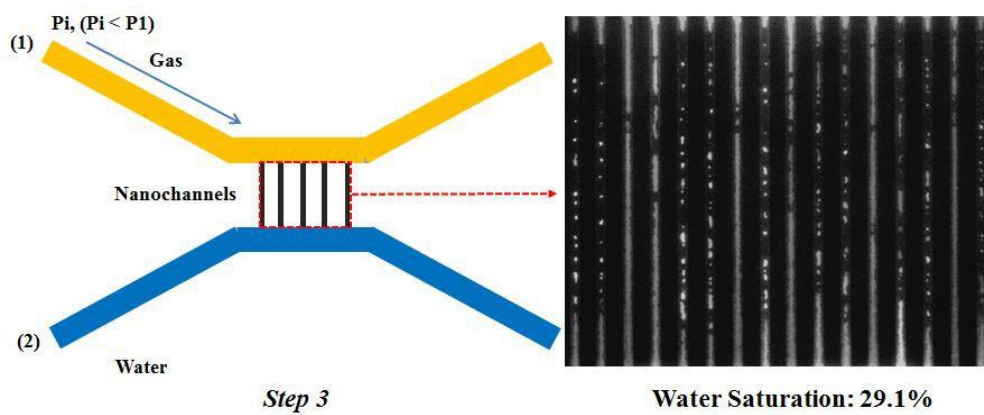


Figure 2-10: Measurement of gas permeability at different water saturation, step 3.

In order to obtain intrinsic relative gas permeability, (apparent) gas permeability



was determined first without the consideration of gas slip effect. Figure 2-11 (a) summarize the correlation between the apparent gas permeability and the reciprocal of mean pressure at a different water saturation ( $S_w$ ) ranging from 0 to 42%. Figure 2-11 (b) shows the correlation between the starting pressure and the obtained remaining water saturation. It was found that the apparent gas permeability has a linear correlation with the reciprocal of mean pressure, at all experimental conditions. There are fewer data points when water saturation was high (42%) because the saturated water stayed immobile only in the range of low mean pressure as discussed above.

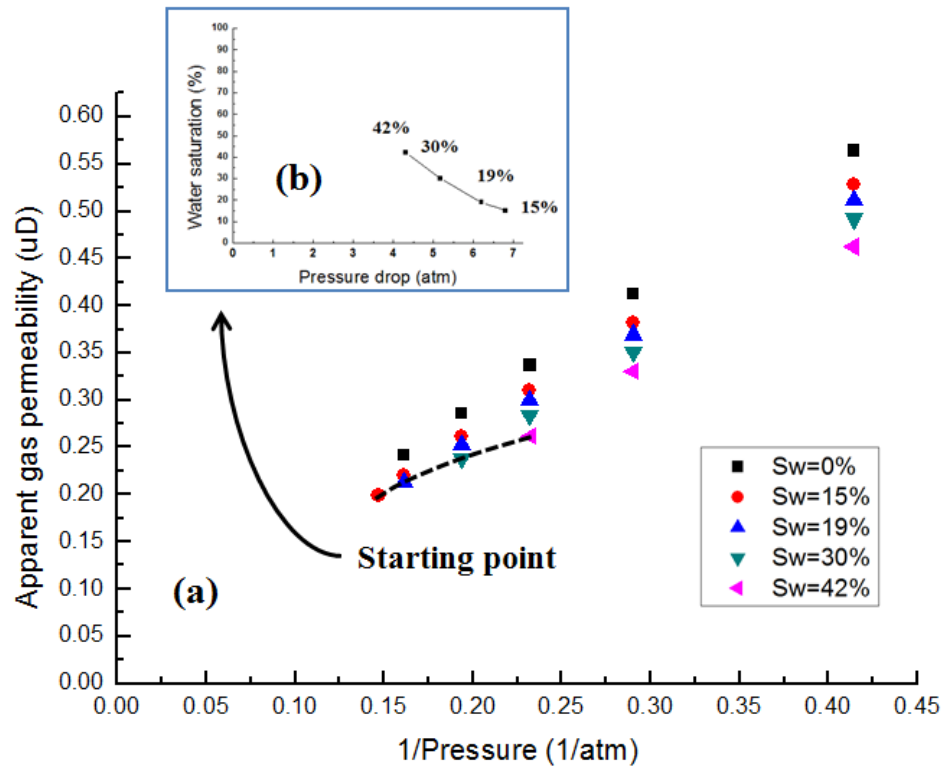
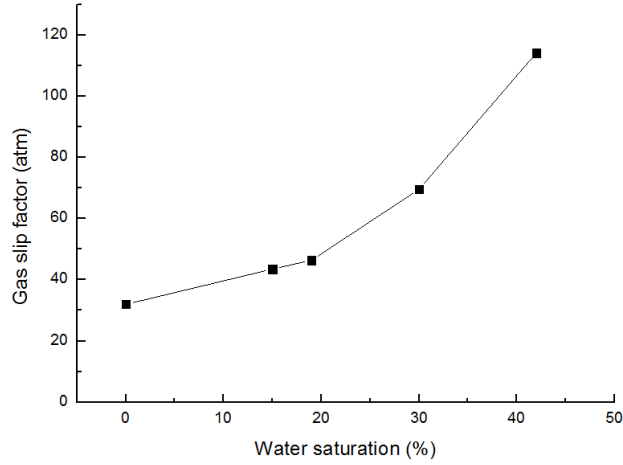


Figure 2-11: Gas slip effect at different water saturations.

The intrinsic gas permeability at different water saturation was obtained by linear regression at infinite pressure ( $\frac{1}{p} = 0$ ) on each curve of experimental data. From the data shown in Figure 2-11, the gas slip factors at different water saturation were calculated and presented in Figure 2-12. It was found that the gas slip factor increased with the increase of water saturation, which is consistent with Klinkenberg theory [49] and results reported from Li et al [39].





**Figure 2-12: Correlation between water saturation and gas slip factor.**

As mentioned in the introduction part, there are a few researchers reported [38, 41, 42] that gas slip factor decreases with the increase of water saturation. There are many possible reasons for this contradiction, such as the geometry and pore structure of the samples, method to establish the liquid saturations, and distribution of the water saturation.

Here we suggest the major reason could be the distribution of the water saturation. Based on the observed flow patterns, in each of the three types of flow pattern, the nanochannel was occupied by both the gas and the water phase. This phenomenon indicates that the gas displacing water experiments in this study fall into the funicular flow regime. Since the water phase either occupied one side or the both sides of the channel in the form of a water layer, it is clear that the existence of the water layer has reduced the radius of gas flow in the nanochannels. According to Klinkenberg's theory in Eq. 2.11, the slip factor is inversely proportional to the effective radius of the flow, and thus increases with the increase of water saturation.

The remaining water saturation across the test section was also obtained by analyzing the imaging data. The water saturation in each single nanochannel is calculated and distribution results are summarized in Figure 2-13. It was found that overall the saturated water in the nanochannel is randomly distributed across the whole test section, especially for high water saturations. The possible reason of the random distribution of saturated water might attribute to the slight nonuniformity of the nanochannels.

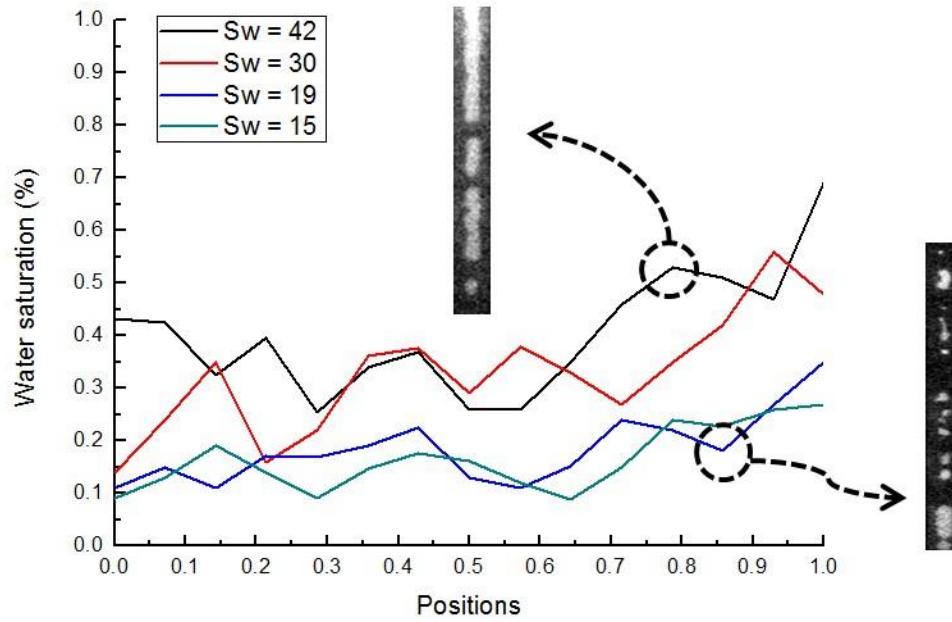


Figure 2-13: Distribution of water saturation in nanochannels.

### 2.7.3 Water displacing gas in nanochannels

Water displacing gas experiments were also conducted in the nanochannels. The nanochannels were 100% saturated with nitrogen gas and no water was observed in the test section. Then a water phase with fluorescence dye was injected into the nanochannels. The water pressure drop ranged from 0.8 psi to 57.5 psi. The flow rate, flow pattern and gas saturation were obtained from the imaging data. Figure 2-14 shows the displacement pattern of water phase displacing gas in nanochannels before the break through (unstable stage). Frontal displacement (piston-like) was observed in most cases. This is because each nanochannel is one independent straight channel and the cross sectional area is uniform. When the pressure drop is relatively low, a specific displacement pattern – liquid slug with cavity on the side is observed. In this pattern, water does not occupy the entire nanochannel. A liquid core is formed with gas at the edge of the channel.

Overall, gas residual saturation in nanochannels is very low (<10 %) under all experimental conditions. The major reason is that the inner surface of channels is hydrophilic. Another reason might attribute to the geometry features of nanochannels: the aspect ratio of cross section is relatively high (width / height = 50). When reach to small dimensions, the rigidity of gas bubble is relatively high and gas bubbles will try to keep the spherical shape to reduce surface tension. The nanochannels in our experiment are too wide for gas bubble to occupy the entire cross-section.

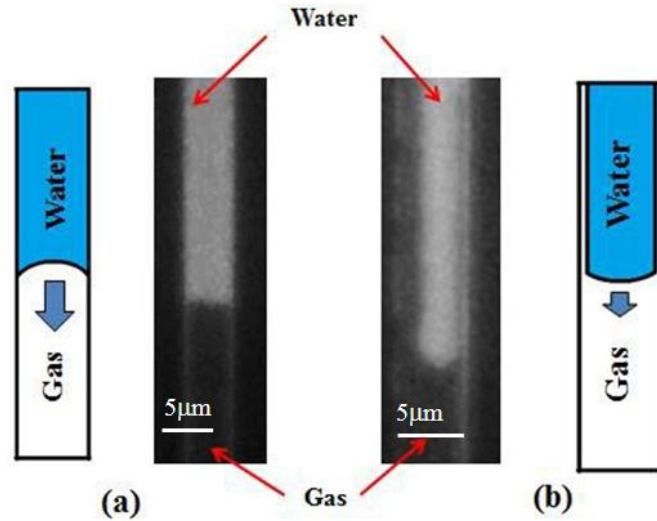


Figure 2-14: Water displacing gas patterns, two different interfaces patterns.

(a) A frontal displacement interface under pressure drop of 12.5psi; (b) a liquid plug with cavity under pressure drop of 0.8 psi.

## 2.8 Conclusions

Displacements of two-phase flow in 100 nm-deep fractures were characterized. Specifically, the two-phase gas slippage effect was investigated. Under experimental conditions, the gas slippage factor increased with the increase in the water saturation, possibly because the water saturation increase dramatically reduced the effective radius of the gas channel. Based on Klinkenberg's theory, the gas slippage factor increases as the channel radius decreases, which was proved by the two-phase flow imaging data.

## 2.9 Future experimental plan

Two phase flow behavior in nanochannels will be continuously investigated by using newly fabricated nanofluidic chips and nano-scale network models. The gas slippage effect and residual fluid saturation will be characterized.

### **3. The Flow Behavior of Friction Reducer in Microchannels during Slickwater Fracturing**

#### **3.1 Summary**

Slickwater fracturing has been proved to be an effective method to increase the shale gas productivity. Friction reducer is a primary component of slickwater used to decrease the flowing friction in wellbore during hydraulic fluid pumping. Lab tests and field applications have addressed this issue thoroughly. However, the fluid will be pumped into formation and the flow characteristics of this solution in microfractures existing in the formations are not clear. This study used capillary tubes to represent microfractures and the flow behavior of friction reducer solution in capillary tubes was systematically studied. Results show that friction reducer increased water flow resistance in microfractures by up to 20% rather than reduced flow friction as it acted in wellbore tubings. The resistance increased with the decrease of flow rate. The existence of friction reducer in microfractures resisted water flow by a factor of 1.2.

#### **3.2 Introduction**

Tight formations with extremely low matrix permeabilities can produce at economical rates primarily because of inborn fissures and the hydraulic fractures created in formation during hydraulic stimulation. A hydraulic fracturing treatment in shale gas can connect/generate the inborn and introduced microfractures, causing them to become much more complex fracture networks than a pair of main fractures. The fracture networks will expose more matrix as the number of micro-sized fractures increases [52-55]. Among the various fracturing methods, slickwater fracturing has been proved to be an effective method by which to increase the recovery of shale gas reservoirs [56, 57]. By adding a very small amount of chemical to the fluid (<1 vol% of the liquid volume), slickwater fracturing fluid can lower the surface pumping pressure below that achieved with the traditional cross-linked fracturing fluid. The slickwater fracturing fluid also demonstrates a relatively low viscosity, which significantly reduces the gel damage during hydraulic stimulation. In order to carry proppant in this low-viscosity fluid, higher pump rates usually are required. Therefore, the friction through the pipeline and the associated energy loss could be significant. Friction reducer (FR) is a primary component of this fluid. Most of the common FRs are polyacrylamide-based polymer, usually manufactured as water-in-oil emulsions and added to the fracturing fluids (hydration) "on the fly." It minimizes energy loss by changing turbulent flow into laminar flow via interactions with turbulent eddies, thereby decreasing the flow friction in macro tubing [58, 59]. Flow loop tests in the laboratory [60-66] and field applications [67-71] have addressed this phenomenon well, showing 10% to 85% friction reductions in the lab and 30% to 90% in the field, respectively, compared with that of fresh water. During a slickwater fracturing treatment, a pair of main fractures firstly is generated perpendicular to the wellbore direction. As the fluids continue to pump, more micro-

sized fractures are generated near the main fractures. These microfractures have much more contact area with the matrix and therefore hold the majority of the productivity potential of shale gas [52, 53, 72]. However, the flow characteristics of FR solution in these microfractures are not clear. The present study attempts to represent how this FR solution flows in microfractures by considering how it flows in microchannels. A commercial FR was prepared with deionized water at a very low concentration. The size of the particles in the FR solution first was analyzed, ranging from the macro- to the nano- meter. Then, the FR solution fluxed the microchannels with various velocities. The effects of solution concentrations, microchannel size wettability, and shear rates on injection pressure were investigated in details. Finally, the experimental results were compared with field data, and their impact on the gas shale matrix was analyzed.

### 3.3 Experiment

#### 3.3.1 Materials

Friction reducer: A commercial polyacrylamide-based polymer, FR, was used for the study. Deionized (DI) water was used to prepare the FR solutions with four concentrations: 0.025, 0.05, 0.075, and 0.1 vol%, according to standard industry practice. Circular capillary tubes, used as a representative of microchannels, were made of fused silica and purchased from Polymicro, Phoenix, AZ. The products label that the nominal inner diameters are 25  $\mu\text{m}$ , 48.6  $\mu\text{m}$  and 102  $\mu\text{m}$ , respectively. However, in order to achieve more reliable data, the inner diameters of these capillary tubes were examined with a Helios Nano Lab 600 Scanning Electron Microscope (SEM) (FEI, Hillsboro, OR). Figure 3-1 depicts the cross-section view of a capillary tube with a labeled diameter of 102  $\mu\text{m}$ , and it is found that the actual inner diameter is 103.43  $\mu\text{m}$ . The difference between the nominal and actual diameter is seen frequently in the experimental studies related to capillary tubes [73, 74].

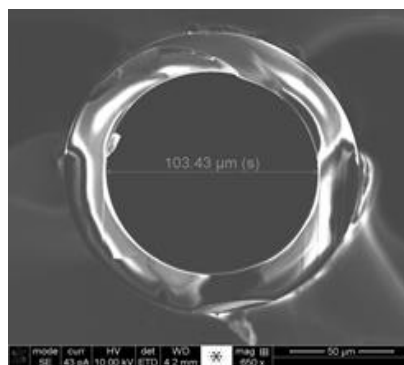


Figure 3-1: Microchannel cross-sectional diameter examined with SEM.

The inner surfaces of the capillary tubes are hydrophilic [75-77]. In order to study the wettability effect, the insides of some of the capillary tubes were coated with a thin (preferably monomolecular) layer of a hydrophobic, non-ionic polymer according to the following coating procedures [78]:

- 1) Rinse the capillary tubes with 1 mol/L HCl, 1 mol/L NaOH and methanol for 5 minutes;
- 2) Fill the capillary tubes with methanol and 3-(trimethoxysilyl)propyl methacrylate mixture (1:1), and incubate at room temperature for 15 hours;
- 3) Flush the capillary tubes with methanol and DI water;
- 4) Fill the capillary tubes with acrylamide reaction reagent, and keep the reagent in the capillary tubes for 2.5 hours;
- 5) Flush the capillary tubes with DI water and Nitrogen for 10 minutes.

The diameters of all capillary tubes were examined by SEM and listed in Table 3-1.

Table 3-1: Microchannel Parameters

Nominal	Actual		
ID (Hydrophilic), $\mu\text{m}$	ID (Hydrophilic), $\mu\text{m}$	ID (Hydrophobic), $\mu\text{m}$	Length, $\mu\text{m}$
25	26.29	26.22	7.5
48.6	52.25	51.56	14.58
102	104.06	103.43	30.6

### 3.3.2 Equipment

The apparatus used in the experiment consisted of a pump, a digital pressure gauge, two non-piston accumulators, microchannel inlet assemblies, and a data acquisition system, as shown in Figure 3-2. A high-pressure ISCO 500D syringe pump (Teledyne Technologies, Thousand Oaks, CA) provided the fluid driving power, with a flow rate ranging from 0.001-204 mL/min. The digital pressure gauge (Keller, Winterthur, Switzerland) measured the microchannel inlet pressure over a pressure range of 0-30 MPa with an accuracy of  $\pm 0.1\%$ . To minimize the friction in the flow line, two non-piston accumulators (Swagelok, Solon, OH) were used. Decane (Fisher Science, Waltham, MA), a nonpolar liquid that will not dissolve in water, was employed to fill the pump so that it could work as a driving fluid to push the DI water and FR solution, respectively, from the accumulators into the microchannels. The microchannel inlet was checked to ensure that it was tight enough to hold the maximum inlet pressure before each experiment. The data acquisition system was connected to the digital pressure gauge to collect the pressure data over time. A dynamic light-scattering particle size analyzer U1732 (Nanotracs, Montgomeryville, PA) was used to characterize the FR solution emulsion particle size distribution. All experiments were carried out at room temperature.

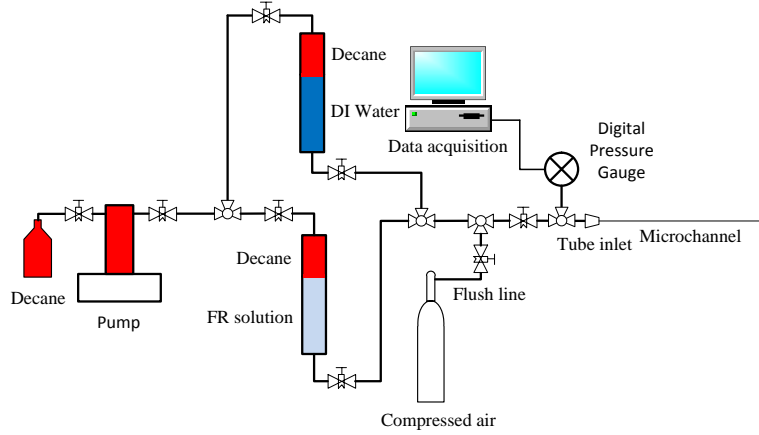


Figure 3-2: Schematic diagram of experiment.

### 3.3.3 Procedure

The pump cylinder was filled with decane first and allowed to sit for two hours. Then, the decane was pumped into the infill line at a low flow rate until no more gas bubbles came out. The infill line valve then was closed, and accumulators were filled with DI water and FR solution, respectively, with a syringe. To ensure that no more gas bubbles existed, the fluids were stirred with a clean glass stick. The entire flow line was checked before running the experiments to prevent any future gas bubbles or leaking. Each experiment used a new microchannel. Due to the fragility of the fused silica during cutting, equal lengths cannot be guaranteed. A difference of a few millimeters may exist. Therefore, the pressure gradient is used in the Results and Discussion sections.

Based on the flow rate and the inner diameter of the microchannels, the fluid velocity was calculated by:

$$v = \frac{4q}{\pi \times D^2} \quad (3.1)$$

Where  $v$  is the fluid velocity in ft/s;  $q$  is the fluid flow rate in ft<sup>3</sup>/s; and  $D$  is the inner diameter of the microchannel in ft.

During one experimental run, the following five fluid velocities were implemented in each microchannel: 11.4-12.6, 5.7-6.3, 2.8-3.2, 1.4-1.6, and 0.3 ft/s. The pump was set to maintain the highest flow rate initially. Pressure vs. time was measured. When the pressure was constant within a 0.3% of current reading over a 5-minute period, it was considered as the flow reaching stable state. Then, the next highest flow rate was employed, continuing in this manner until all velocities were tested. The data presented in this paper were all at the steady state. For each experiment, the time, pressure and flow rate were recorded by the data acquisition system.

### 3.4 Results and discussion

The FR polymer was in water/oil emulsion form and the emulsion particle size of the FR



solution first was characterized. Then, eighteen experiments were conducted to study the impact of the FR concentration, microchannel size, wettability and shear rate on the flow behavior of the FR solution and its residual resistance factor to water was also tested at various velocities.

### 3.4.1 Friction reducer solution emulsion particle size analysis

FR is in the form of water-in-oil emulsion. When pumped into a wellbore, the emulsion is reversed and the FR polymer is released by hydrating. The emulsion particle size distribution in 0.05 vol% FR solution was analyzed by a Nanotrak U1732 Particle Size Analyzer. The average results over five tests are shown in Figure 3-3. The solution has two peaks. The left peak indicates that there are particles with a 0.00093  $\mu\text{m}$  diameter of 3.7 vol%. The majority of the emulsion particles lie in the right peak. Their diameters are 0.0723-1.635  $\mu\text{m}$  of 96.3vol%, and the peak diameter is 0.555  $\mu\text{m}$ .

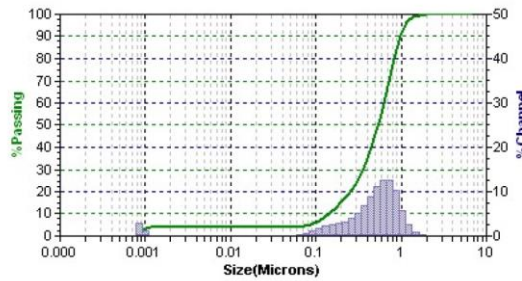


Figure 3-3: Particle size distribution of 0.05 vol% FR solution.

### 3.4.2 Concentration effect on pressure gradient and apparent viscosity

Four concentrations of FR solution were used: 0.025, 0.05, 0.075, and 0.1 vol%. Each sample was injected into a 52.25  $\mu\text{m}$  microchannel. Figure 3-4(a) depicts the effect of FR concentration on pressure gradient and apparent viscosity. A higher concentration solution had a larger pressure gradient at high velocities but the gradient decreased as the fluid velocity decreased. The four lines were approaching to each other at lower velocities. At the velocity of 0.3 ft/s, they were almost identical.

Equation 3.2 can be used to calculate its apparent viscosity,  $\eta_{app}$ :

$$\eta_{app} = c_1 \times K \frac{AdP}{qdL} \quad (3.2)$$

Where  $\eta_{app}$  is the apparent viscosity in cP;  $c_1$  is the conversion factor,  $c_1=7.32 \times 10^{-7}$ ;  $k$  represents the permeability in mD;  $A$  is the cross-sectional area in  $\text{ft}^2$ ;  $dP$  is the pressure drop in psi; and  $dL$  is the microchannel length in ft.



At the same velocity and the same microchannel,  $K$ ,  $A$ , and  $q$  in Equation 3.2, will not change. The apparent viscosity then can be simplified to:

$$\eta_{app} = \frac{(dP / dL)_{FR}}{(dP / dL)_{DIWater}} \quad (3.3)$$

As illustrated in Figure 3-4 (b), the apparent viscosity of the FR solution is always higher than that of DI water ( $1 \times 10^{-3} \text{Pa}\cdot\text{s}$ ). This viscosity is small at a high velocity (11.35 ft/s) and large at a low velocity (0.28 ft/s). This is because FR is polyacrylamide-based polymer, and its solution usually behaviors as non-Newtonian fluid.

The above results indicate that the FR solution had a higher resistance in microchannels than water. The resistance could reduce FR penetration into microfractures during hydraulic stimulation and thus could reduce its damage on formation.

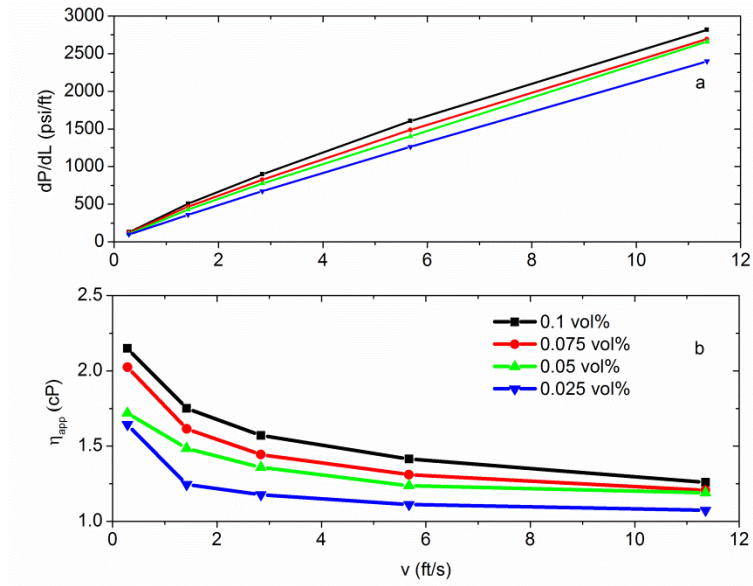


Figure 3-4: Effect of FR solution concentration.

### 3.4.3 Effect of microchannel size on pressure gradient and apparent viscosity

A 0.05 vol% FR solution was used to flux the 104.06  $\mu\text{m}$ , 52.25  $\mu\text{m}$ , and 26.29  $\mu\text{m}$  microchannels at five velocities, respectively. It takes longer for the microchannels with small diameters than those with large diameters to reach a steady state, as shown in Table 3-2.

Table 3-2: Time to reach equilibrium

ID, $\mu\text{m}$	Time, min				
	11.4-12.6 ft/s	5.7-6.3 ft/s	2.8-3.2 ft/s	1.4-1.6 ft/s	0.3 ft/s
26.29	150	120	160	150	170
52.25	23	15	18	17	23
104.06	6	3	3	4	5

Figure 3-5 (a) illustrates that the pressure gradient in small microchannels is larger than that in larger ones. As a velocity decreases, the pressure gradients of the three microchannels become more identical. When comparing this behavior of the FR solution with DI water, as shown in Figure 3-5 (b), the apparent viscosity increases as the velocity decreases. The FR solution in large microchannels has a higher apparent viscosity than that in small ones. Seright [79] reported that Xanthan produces a similar phenomenon, as shown in Appendix A (Figure 3-12). The resistance factor he used ( $Fr$ ) is defined as the ratio of the mobility of the water to the mobility of the polymer. Under the same experimental conditions, the resistance factor equals to the apparent viscosity. With the 55 mD, 269 mD, and 5120 mD cores, at the same fluid velocity, the resistance factor is higher for high-permeability rocks than for low-permeability ones.

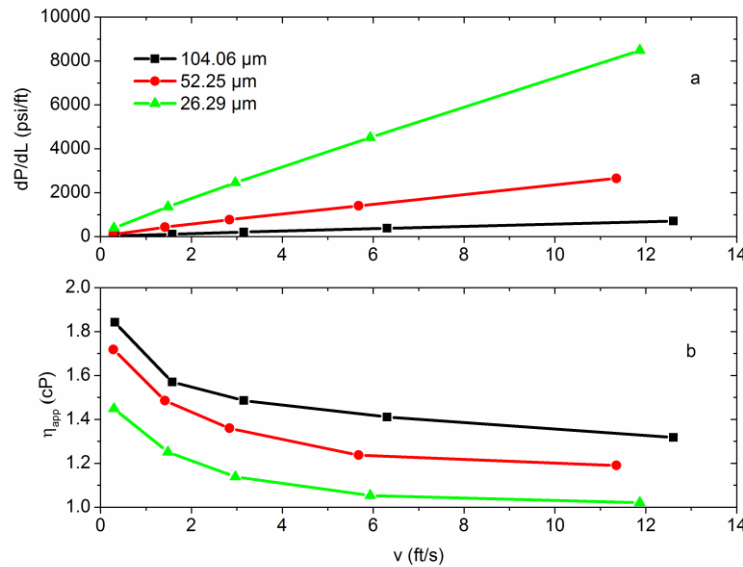


Figure 3-5: Effect of microchannel size.

The Reynolds number gives a measure of the ratio of inertial forces to viscous forces and is used to characterize different flow regimes, such as laminar or turbulent flow. It can be calculated using Equation 3.4:

$$\text{Re} = c_2 \times \frac{\rho v D}{\mu} \quad (3.4)$$

Where  $c_2$  is the conversion factor,  $c_2=1489.6$ ;  $\rho$  is the fluid density in  $\text{lb}/\text{ft}^3$ ;  $D$  is tube diameter in inch; and  $\mu$  is the fluid dynamic viscosity in cP.

The Re is presented vs. velocity with different microchannel sizes in Figure 3-6. Large microchannels have a larger Re at similar velocities, which is consistent with Equation 3.4. In this study, the Re can reach 300, smaller than the transitional Re of 2300, which indicates that the experiments were under a laminar flow regime.

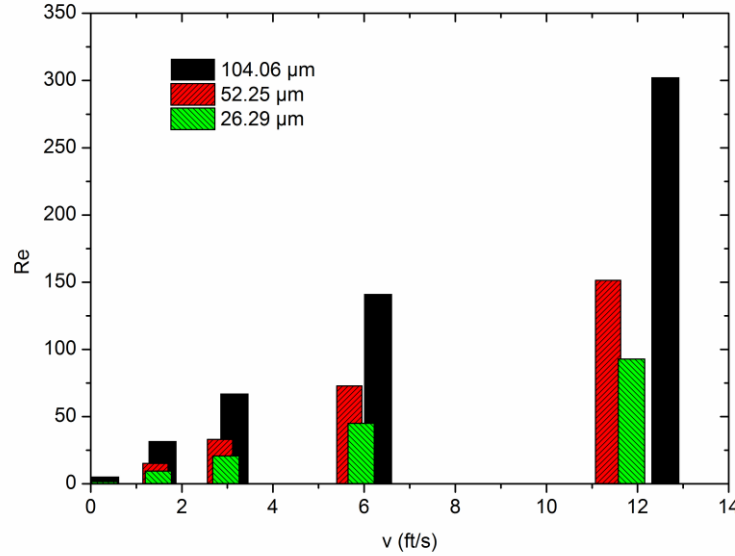


Figure 3-6: Reynolds number vs. velocity.

#### 3.4.4 Wettability effect on pressure gradient and apparent viscosity

With a 0.05 vol% FR solution, experiments were conducted in hydrophilic (52.25 μm, 104.06 μm) and hydrophobic (51.56 μm, 103.43 μm) microchannels. As shown in Figure 3-7, the wettability modification does not affect injection pressure gradient very much. However, when using Equation 3.5, the difference between the hydrophilic and hydrophobic microchannels can be clearly identified, as shown in Figure 3-8. The pressure gradient of the FR solution in microchannels with hydrophilic surfaces is always higher than those with hydrophobic surfaces. At high velocities, the difference is small (<3%), but it increases to 20% as the velocity decreases. The pressure gradient difference in small microchannels is bigger than that in large microchannels, especially at low velocities. In another word, the FR solution is not very sensitive to the surface wettability at high velocities, but this sensitivity increases in smaller microchannels and at lower velocities.

$$\Delta dP/dL = \frac{(dP/dL)_{Hydrophilic} - (dP/dL)_{Hydrophobic}}{(dP/dL)_{Hydrophobic}} \times 100\% \quad (3.4)$$

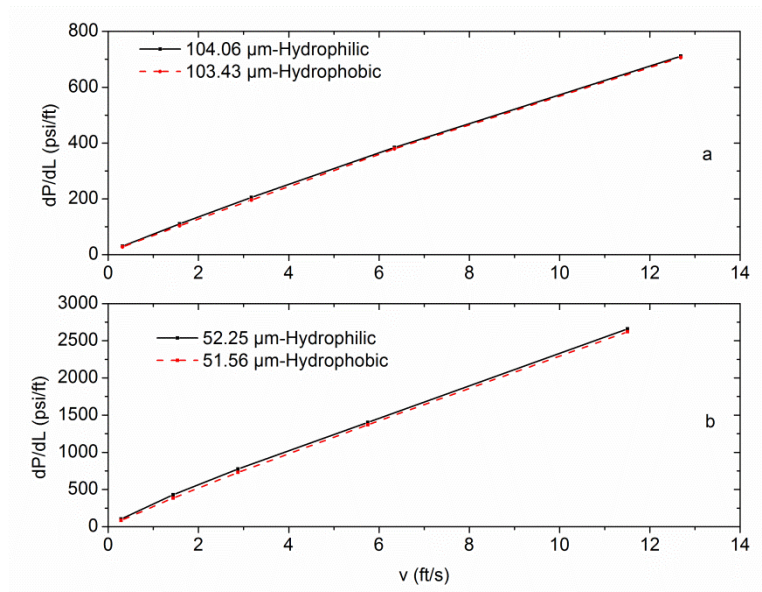


Figure 3-7: Wettability effect.

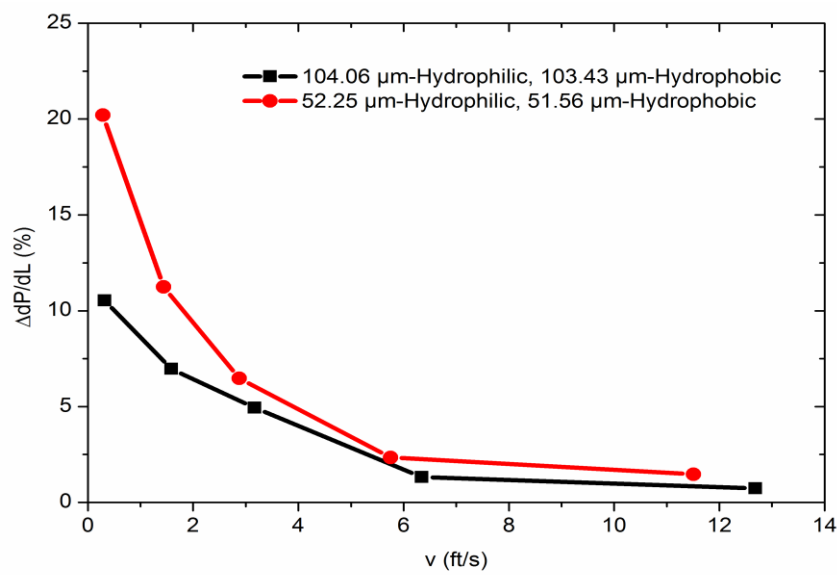


Figure 3-8: Apparent viscosity difference vs. velocity under different wettabilities.

The sensitivity of the FR solution to the microchannel size could be interpreted as follows. A very thin polymer layer (boundary layer) adhered to the inner wall after FR solution was injected. When a fluid flowed in large channels, the boundary layer occupied less portion of the cross-sectional area, thus having less impact on the flowing pressure. In small channels, however, it occupied a relatively large portion of the cross-sectional area. The sensitivity to velocity can be explained by the changing boundary layer thickness. This thickness was affected by the fluid velocity in the channel and the surface wettability condition. Due to the interaction between the shear force provided by the driving fluid and the fluid's internal resistance, the boundary layer would be thicker at

low fluid velocities and at high fluid velocities, as shown in Figure 3-9. A thick boundary layer would result in a smaller flow path diameter and would require higher pressure for a fluid to pass through, and vice versa for a thin boundary layer.

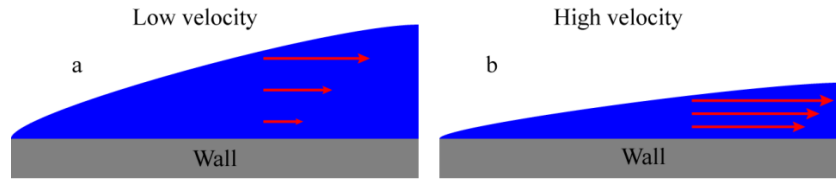


Figure 3-9: Boundary layer change with velocity.

### 3.4.5 Shear rate effect on pressure gradient and apparent viscosity

The shear rate is the velocity gradient measured across the diameter of a fluid flow channel. It is the rate change of velocity at which one layer of fluid passes over an adjacent layer. 0.05 vol% of FR solution was used to flux the 104.06  $\mu\text{m}$ , 52.25  $\mu\text{m}$  and 26.29  $\mu\text{m}$  microchannels, respectively. As Figure 3-10 depicts, the apparent viscosity of the FR solution decreases with the increase of shear rate. At a same shear rate, the FR solution in larger microchannel displays a higher apparent viscosity.

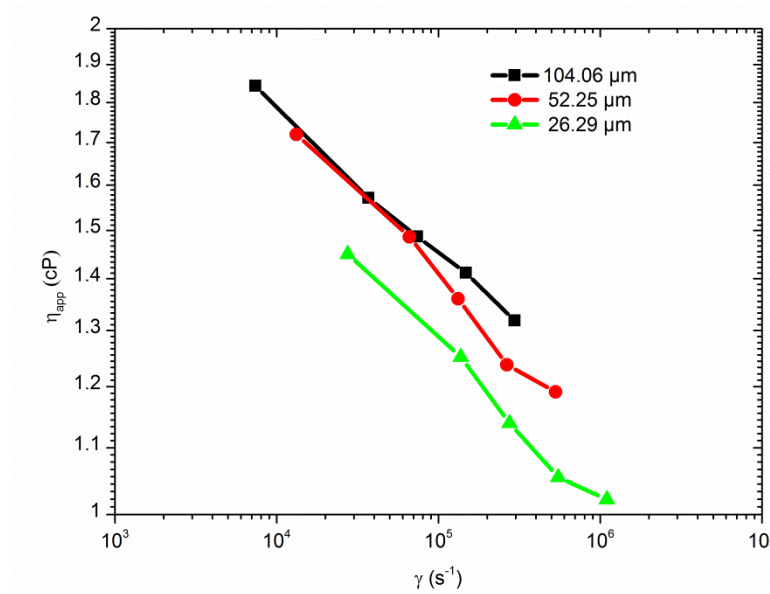


Figure 3-10: Shear rate effect on apparent viscosity.

Based on the relationship between the common shear rate and apparent viscosity, for the same fluid, the three curves should be on the same line. However, Xanthan, which is also a shear thinning polymer, fluxes in 55 mD, 269 mD, and 5120 mD rock [79]. Under the assumption that the rock is homogeneous, the permeability data were converted to circular capillary diameters, as shown in Appendix B (Figure 3-13). Then, the velocity was converted to shear rate. Figure 3-13 shows the shear rate vs. the resistance factor, indicating that the large capillary has a larger resistance factor at the same shear rate, which is consistent with Figure 3-10. Blood is also a shear thinning fluid; when it flows in

different gaps between the shearing plates, a similar phenomenon occurs [80], as shown in Appendix C (Figure 3-14).

### 3.4.6 Residual resistance factor to water

The chemical residual condition after stimulation is closely related to the fracturing fluid flowback and gas production rate. The residual resistance factor,  $F_{rr}$ , is often used to describe how rock permeability is changed after a chemical treatment.  $F_{rr}$  is defined as follow:

$$F_{rr} = \frac{M_b}{M_a} = \frac{(k/u)_b}{(k/u)_a} \quad (3.6)$$

Where  $M$  is the fluid mobility in  $\text{mD}/(\text{cP})$ ; and  $b$  and  $a$  represent water flows before and after the FR solution, respectively.

If  $F_{rr}$  equals to 1, then the fluid flow after polymer injection will not be affected. In this case, the FR solution would easily flow back to the main pair of fractures and will not impair the fluid flow.

In this study, DI water was used to flux the microchannel before and after 0.05 vol% FR solution. With Darcy's equation, Equation 3.6 can be converted into Equation 3.7.

$$F_{rr} = \frac{\Delta P_a}{\Delta P_b} \quad (3.7)$$

Figure 3-11 gives the residual resistance factor as a function of velocity. The residual resistance factor is low (1.02) at high velocity and high (1.38) at low velocity. This is due to the viscous property of FR solution. As a polymer solution, it will always leave some amount of fluid behind after flooding. For microchannels of the same size, at a high velocity or high shear rate, the fluid has high mobility and low apparent viscosity (Figure 3-10); therefore, it could be flushed out easily. The exact opposite is true under conditions of low velocity and low shear rate.

Smaller microchannels have larger residual resistance factors at the same velocity and surface wettability. At the same velocity, the boundary layer thickness occupies a large portion of the cross-sectional area in small microchannels and a small portion of large ones. If the fluid is flowing at the same velocity, when using DI water to push FR solution out, higher pressure is required for small microchannels. Gas shale is characterized by nano-sized pores and throats. It is more difficult for the fluid in small microchannels to flow back. This explains why gas shale reservoirs demonstrate low fluid flow back after hydraulic fracturing. Polymers/gels are widely used in mature oil/gas fields for water shutoff [81-83]. Their fracture experiments show hundreds to thousands of residual resistance factors. However this FR solution has a very small  $F_{rr}$  (1.02-1.38). The FR solution will not easily block the micro-sized flow path. It will easily flow back and therefore cause little impairment to microfractures.

The residual resistance factor at the hydrophobic surface is always approximately 0.05 higher than that at the hydrophilic surface because the FR solution has a strong hydrophilic property, and the boundary layer thickness in hydrophilic microchannels makes contact with more of the cross-sectional area than the hydrophobic ones. Additionally, the relatively small flow path diameter requires higher pressure at the same velocity.

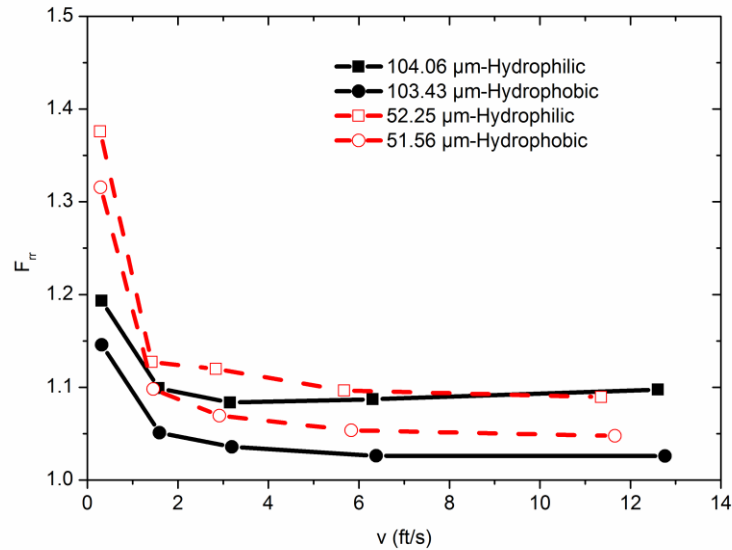


Figure 3-11: Residual resistance factor of different microchannels.

### 3.4.7 Data comparison with flow loop experiment

In 0.677 in, 0.9 in, and 1.162 in macro tubings, flow loop experiments were conducted with the 0.075 vol% FR solution (71). At a fluid velocity around 10 ft/sec, the injection pressure decreased around 40% compared with water. The net treating pressure ( $P_{\text{net}}$ ) is the differential pressure between borehole bottom pressure and reservoir pressure. It usually requires 600-1000 psi (4.1-6.9 MPa) net treating pressure to create fractures for shale gas reservoirs [84, 85]. In our experiments, the injection pressure of FR solution into a 52.25  $\mu\text{m}$  microchannel reached to  $P_{\text{net}}$  (1000 psi) at the velocity of 11.5 ft/s as shown in Fig 3-5, which is similar with the fracturing fluid flow velocity during stimulation but the injection pressure did not decrease but rather increased 20% comparing to DI water. This means that when FR solution flows in a wellbore, it can reduce friction. When it enters a microfracture, it will increase friction due to the restricted dimension. In another word, the fluid will not easily penetrate into the microfractures and thus can produce less damage on the gas flow of microfractures after production.

### 3.4.8 Potential impact of FR solution on the shale matrix



Shale gas is stored in shale formation and composed of “free” compressed gas in pores and fractures and adsorbed gas in organic kerogen of the rock [86], which usually has very low porosity [87, 88]. After hydraulic fracturing, the extension of the microfractures to the gas-rich kerogen, comparing with the reservoir pressure, there would be a pressure drop. Once this pressure drop gradient is high enough, gas would be desorbed from the kerogen and begin to flow to the microfractures [89]. At the same time, if the matrix pore is filled by hydraulic fluid, an additional pressure gradient would be required. If this pressure gradient is too high, the gas reservoir may not produce anymore, thereby requiring further improved gas recovery methods.

The pore size of typical gas shale usually ranges from 0.1 to 0.005  $\mu\text{m}$  [90]. When compared with the emulsion particle size distribution of the FR solution, there is only a small overlap, less than 5%. Regarding pore size, according to Philip H. Nelson [90], only Pennsylvanian shales can reach up to 0.1  $\mu\text{m}$ ; Pliocene shales, source rocks, Devonian shales, and Jurassic-Cretaceous shales range only from 0.008-0.07  $\mu\text{m}$ , which region hardly overlaps with the FR solution. Therefore, such friction reducer solution will not easily go into the pores, but it might block the pore entrance to build a filter cake to prevent the fluid from leaking off. Sun’s experiments also confirmed that the FR solution reduced the shale permeability by around 20%. However, with the addition of a breaker, their permeability recovered 100% [67].

### 3.5 Conclusions

Eighteen experiments were conducted to study the effects of concentration, microchannel size, wettability, shear rate on FR solution flow through micro- channels and residual resistance factor to water. Then, the experimental results were compared with the flow loop experimental data conducted in macro tubings. This FR solution impact on the gas shale matrix has been discussed. The major findings are summarized as follows:

- 1) FR solution is a shear thinning fluid. At the same shear rate, the apparent viscosity is higher in larger microchannels.
- 2) The impact of the concentration of FR solution on the flow behavior was more obvious at low velocities. Higher concentrations of FR solution displayed a larger pressure gradient. FR solution displays a strong hydrophilic property, especially at high velocities.
- 3) FR solution is sensitive to the surface wettability at in smaller microchannels and lower velocities, and this sensitivity decreases at higher velocities and larger channels.
- 4) With similar velocity experiments in flow loops and similar net treating pressure in the field, the fluid flow in microchannel experiments were under laminar flow regime, instead of turbulent flow in flow loop. The same friction reducer did not decrease injection pressure, but increased 20%.
- 5) The residual resistance factor is very low for this friction reducer. However, at the same velocity and surface wettability, smaller microchannels have larger residual resistance factors.
- 6) The emulsion particle size in the FR solution was analyzed to be 0.0723-1.635  $\mu\text{m}$ . Compared to typical gas shale pore size, this FR solution emulsion particles will not go into the matrix pores easily, but can block the pore entrance to build a filter cake, and



prevent the fluid from leaking off, and protect the formation from damage during slickwater fracturing.

## Appendix

### 3.6.1 Appendix A

Graph is from Seright et al. [77].

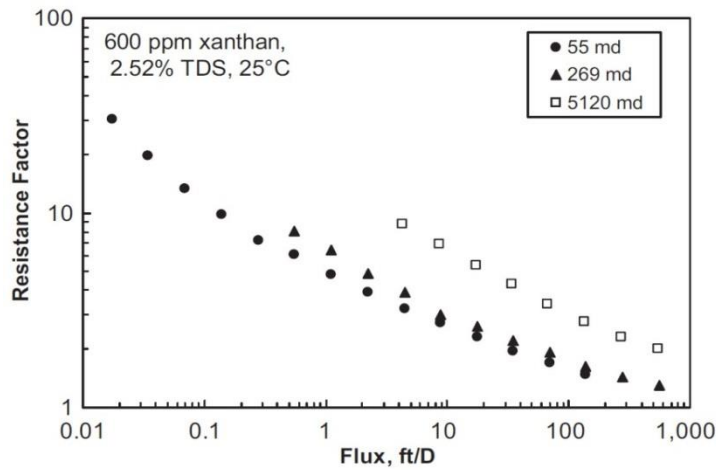


Figure 3-12: Resistance factor vs. flux for 600 ppm Xanthan.

### 3.6.2 Appendix B

Data and graph calculated from /based on Figure 3-12 [77] .

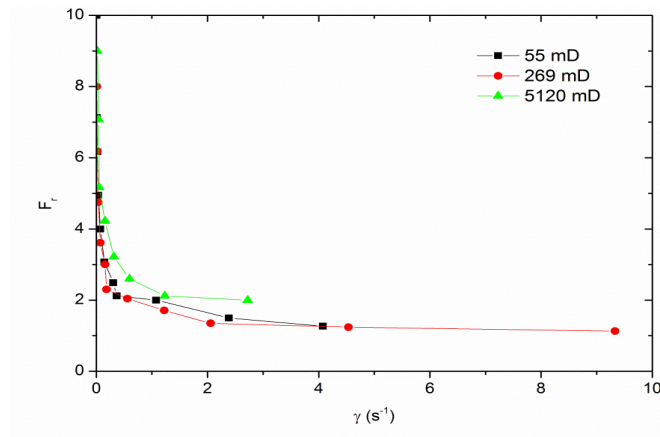


Figure 3-13: Resistance factor vs. shear rate for 600 ppm Xanthan.

Table 3-3: Permeability to capillary diameter conversion

K	$\Phi$	D
---	--------	---

mD		$\mu\text{m}$
55	0.17	10.22
269	0.212	20.23
5120	0.35	68.69

### 3.6.3 Appendix C

Graph reproduced from Bitsch et al[88].

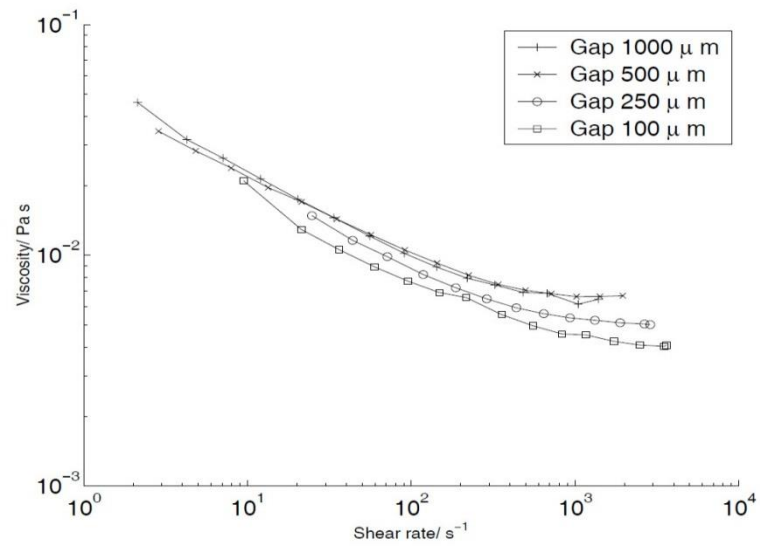


Figure 3-14: Blood flows in different gaps between the shearing plates.

### 3.6 Nomenclature

$a$	=	DI water flux the microchannel after FR solution
$A$	=	Cross-sectional area in ft <sup>2</sup>
$b$	=	DI water flux the microchannel before FR solution
$c_1$	=	conversion factor, $c_1=7.32\times 10^{-7}$
$c_2$	=	conversion factor, $c_2=1489.6$
DI water	=	Deionized water
$dP/dL$	=	Pressure gradient in psi/ft
FR	=	Friction reducer
$F_r$	=	Resistance factor
$F_{rr}$	=	Residual resistance factor
$ID, D$	=	Inner diameter of microchannel in $\mu\text{m}$
$k$	=	Permeability in mD
$L$	=	Microchannel length in ft
$M$	=	Fluid mobility in mD/(cP)
$P_{net}$	=	Net treating pressure in psi
$q$	=	Fluid flow rate in ft <sup>3</sup> /s
$Re$	=	Reynolds number
SEM	=	Scanning Electron Microscope
$v$	=	Fluid velocity in ft/s
$\Delta P$	=	Pressure drop in psi
$\Delta dP/dL$	=	Pressure gradient difference in psi/ft
$\mu$	=	Fluid dynamic viscosity in cP
$\gamma$	=	Shear rate in s <sup>-1</sup>
$\rho$	=	Fluid density in lb/ft <sup>3</sup>
$\eta_{app}$	=	Apparent viscosity in cP

### 3.7 Unit Conversion

1 psi	=	$6.895\times 10^3$ Pa
1 inch	=	0.0254 m
1 ft	=	0.3048 m
1 $\mu\text{m}$	=	$10^{-6}$ m
1 cP	=	0.001 Pa·s

## 4. Numerical Simulation

### 4.1 Summary

The objective of this work is to develop a multiphase flow numerical model to simulate the invasion of hydraulic fracturing fluid into nanopores and the flow back driven by formation pressure. In the first year of the project, we successfully develop a parallelized, 3D lattice Boltzmann simulator capable of simulating multiphase flows; in this second year, we implemented a transport module in the simulator. Specifically, in the second year, we wrote tracer-based algorithms for heat and mass transfer in random geometries made up by spheres. We also calculated the tortuosity of two-dimensional random porous media models made up by channels using lattice-Boltzmann-based methods. These methods, now proven effective, are being implemented to the established three-dimensional parallelized lattice Boltzmann framework. Finally, to extend the capability of the lattice Boltzmann to the slip flow regime, a preliminary work has been conducted to obtain the analytical solutions and the results are included in this annual report.

### 4.2 Tracer-Based Transport Simulations

Pore-scale solution of solute transport may be achieved by direct solution of the advection-diffusion equation or simulation of random-walk of tracers. In tracer-based methods, solute transport is represented by the Brownian motion of discrete tracer particles

$$r_j(t + \Delta t) = r_j(t) + u\Delta t + \xi\sqrt{6D\Delta t} \quad (4.1)$$

Where  $r_j$  is the location of tracer  $j$ ,  $u$  is the fluid velocity,  $D$  is the diffusivity of the solute, and  $\xi$  is a unit vector with a random orientation. By adjusting the magnitude of the diffusivity  $D$  relative to the characteristic flow velocity, transport processes with different Peclet numbers can be simulated. This method has been widely used to simulate mass transport in porous media [91] and more recently in flowing suspensions of particles [92]. For mass transfer simulations, the tracers do not interact with the pore wall when the collisions between tracers and the pore-wall are modeled as specular reflections (Figure 4-1, also [93]). Susp3D [94, 95] is a three-dimensional lattice-Boltzmann program for particulate flows. When particles are packed, they form a representation of a porous medium (Figure 4-2). Due to the simplicity in implementing collision and reflection with spheres, we first modified Susp3D to allow tracers be used to simulate mass diffusion. We then developed the program further to allow tracers to penetrate the pore wall and freely diffuse in the solid particles; this corresponds to the case with solid phase diffusion or heat diffusion. [96] This program will be used to generate data needed for verification, as the tracer-based method is implemented to more complex pore geometries using the lattice Boltzmann framework developed in the first year of this study.

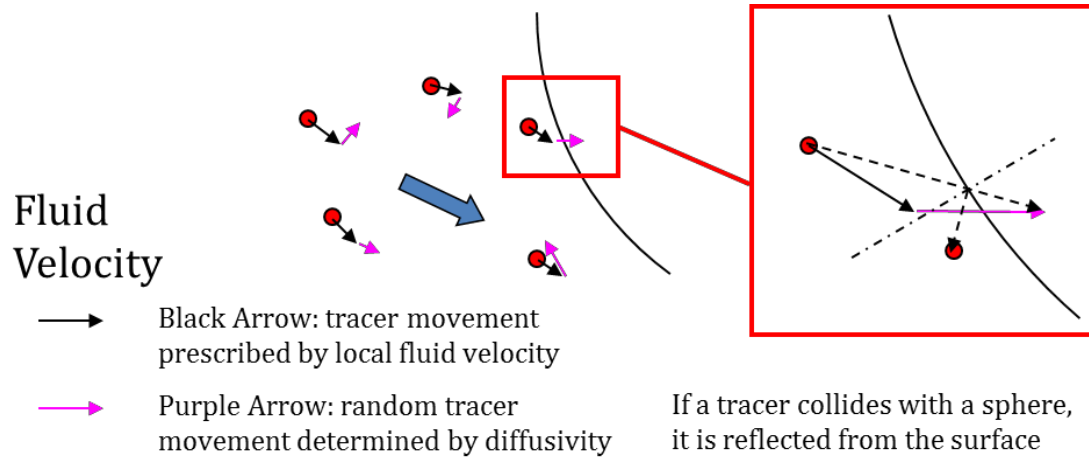


Figure 4-1: A schematic of the tracer algorithm showing the advection-diffusion process of tracers and implementation of specular reflection on a pore wall.

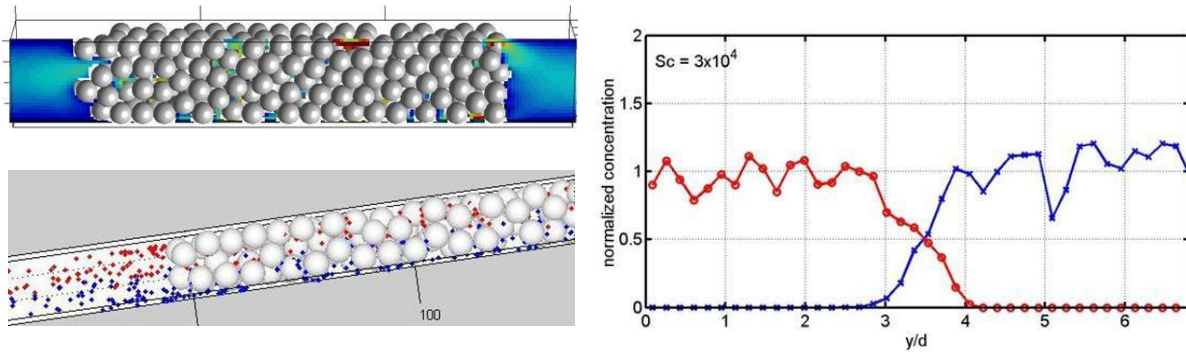


Figure 4-2: Axial velocity distribution of a flow through a packing of spheres (upper left).

In this velocity field, red and blue tracers were released into the upper and lower halves of the packing (lower left) and their mixing level was assessed at the outlet (right).

### 4.3 Direct Solution of the Transport Equation and Tortuosity

Another approach to obtain the dispersion of solute in porous media is to directly solve the advection-diffusion equation. In the absence of flow, the advection-diffusion equation is reduced to a diffusion equation, the solution of which yields the tortuosity of porous media. To supplement and verify tracer-based simulations and to test the effect of complex geometry, we applied a link-type two-relaxation time (LTRT) lattice Boltzmann method [97, 98] to two-dimensional random porous media models and characterized the tortuosity. Because these models are also being used for the microfluidic and nanofluidic studies, this study also provided data that are useful for the experiments.

First, we generated two-dimensional porous media geometries that are homogeneous and heterogeneous (Figure 4-3). These geometries cover a range of porosities from 0.2 to 0.6. Then, the diffusion equation in the pore space is solved using the LTRT lattice Boltzmann method. The fluxes through the porous media models (from left to right, driven by a constant concentration difference) were used to obtain the tortuosity of the media. The characterized tortuosity, presented as a function of porosity, is in good agreement with some of the available empirical formulas for tortuosity (Figure 4-4). In addition, we found that the presence of large and isolated pores increased the tortuosity relative to the case without pores at the same porosity, which may be observed in Figure 4-4. The difference, however, is not very significant. Based on these results, the geometries used in the microfluidic and nanofluidic porous media analogs should have a tortuosity of about two.

In conclusion, we have developed tracer-based solution and LTRT lattice Boltzmann solution of the advection-diffusion equation of solutes. In the next year, we will implement the method(s) to three-dimensional porous media geometry models and systematically study tortuosity and dispersion. Comparison between the tracer method and the LTRT lattice Boltzmann method will also allow us to assess the accuracy and performance of the two approaches. While the LTRT method is generally regarded as more accurate, tracer method has better potential to be extended to systems with multiple solutes. The development of the particle transport module in the third year is going to be a natural extension of the tracer method. More specifically, a finite size will be assigned to the tracers. Among the tracers and between the tracers and the pore wall, colloidal force models (charge, van der Waals, etc.) will be implemented to simulate non-hydrodynamic interactions.

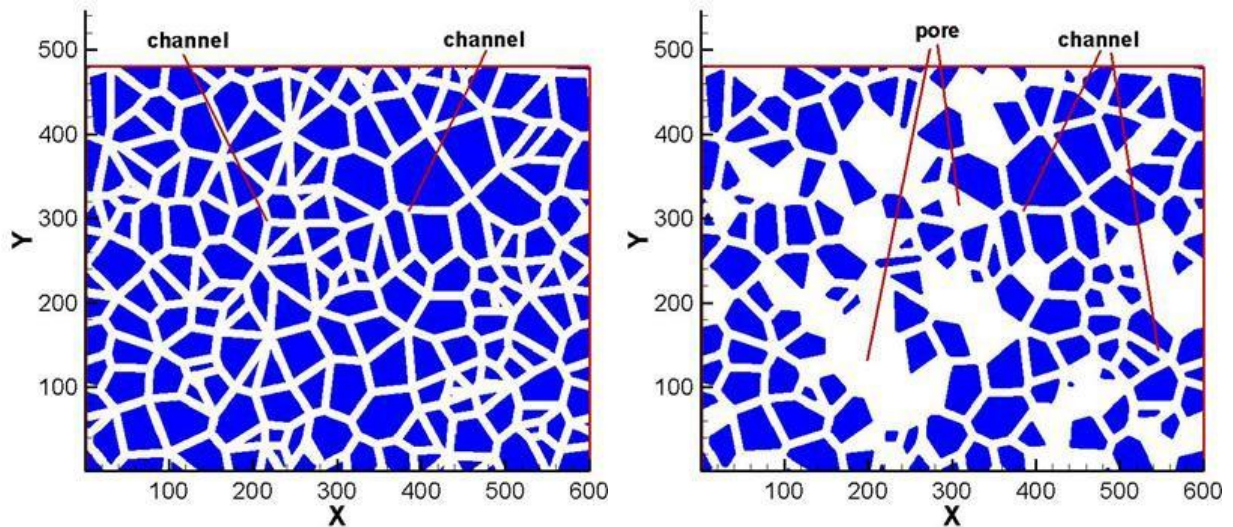


Figure 4-3: Geometry models used for tortuosity calculation.

Left: a homogeneous network made up entirely by channels of the same size; right: a heterogeneous network made up by channels and large pores. These geometries are currently being used in the microfluidic and nanofluidic porous media experimental models.

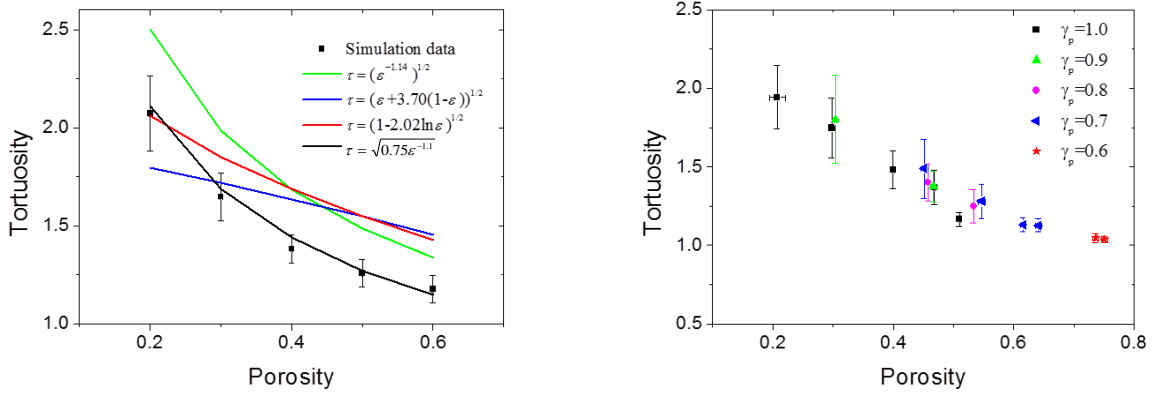


Figure 4-4: Porosity-tortuosity relations for two-dimensional porous media geometry models presented in Figure 4-3.

Left: comparison between the tortuosity of homo-geneous geometries (lines with error bars) and selected empirical formulas; right: tortuosity of homogeneous geometries (black symbols) and heterogeneous geometries (other colors).  $\epsilon$  is porosity and  $\gamma_p$  stands for the fraction of porosity in the channels in the total porosity.

#### 4.4 Analytical and Numerical Solutions for Slip Flows in Simple Geometries

Gas flow in tight gas sand and shale is generally considered to be heavily influenced by non-continuum effects. As the pore size  $d$  approaches the mean free path  $\lambda$  of gas molecules, a Knudsen number may be defined [33]

$$K_n = \frac{\lambda}{d} \quad (4.2)$$

If we assume that the natural gas is mostly made up by methane molecules, calculations typically indicate that natural gas flows through nanosize pores at reservoir pressure and temperature are predominately in the slip flow regime, where the bulk flow still obeys the Navier-Stokes equation, and the no-slip boundary condition on the pore wall in the continuum ( $K_n = 0$ ) limit is replaced by the slip boundary condition

$$U_s = \lambda_s \frac{\partial u}{\partial n} \quad (4.3)$$

Where  $U_s$  is the velocity of the gas at the pore wall,  $\frac{\partial u}{\partial n}$  stands for the velocity gradient on the pore wall, and  $\lambda_s$  is the slip length that may be calculated based on the Maxwell model



$$\lambda_s = \frac{2-\sigma}{\sigma} \lambda \quad (4.4)$$

Here,  $\sigma$  is the tangential momentum accommodation coefficient (TMAC) that takes a value of one if the surface is diffusive and a value of zero if the surface is reflective. True material surfaces generally have TMAC close to one.

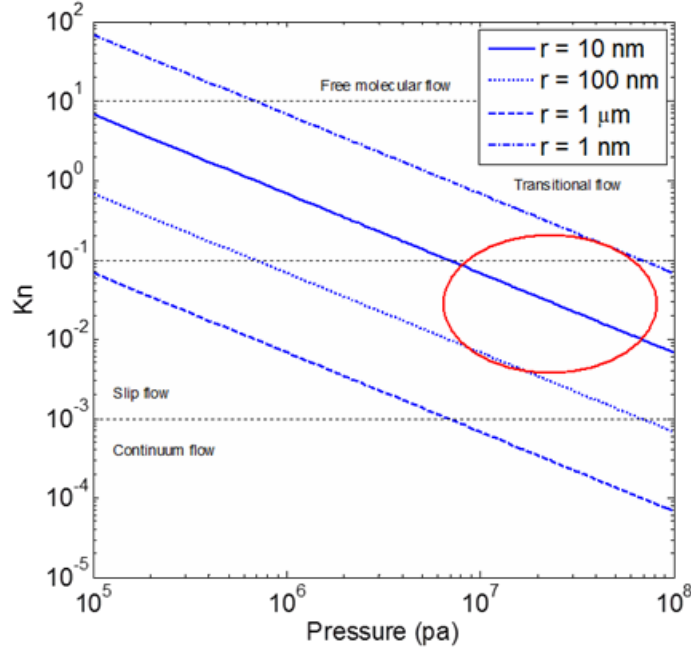


Figure 4-5: Estimates of the Knudsen number at various pressures for four given pore sizes.

The gas is methane with a molecular collision diameter of 0.4 nm. The calculations assume a temperature of 350K. It is observed that when the dominating pore size is about 10 nm, which is indicated by many petrophysical studies of shales [98-100], the distribution of the Knudsen number should largely be in the slip flow regime (highlighted by the red circle).

The lattice Boltzmann framework developed in the first year of this project may be modified to simulate flows with the slip boundary condition. Though not in the scope of this proposal, developing a numerical capability to simulate slip flows in nanopores would allow direct comparison with laboratory measurements of the apparent permeability of cores and the Klinkenberg coefficient, as well as nanofluidic experiments. In order to prepare for this development, we carried out COMSOL simulations of slip flows in a two-dimensional porous media geometry made up by a cubic array of cylinders and analytical derivations for fractures, cylinders, and channels of rectangular cross sections. The results of these studies are presented below.

COMSOL simulations were conducted in the geometry show in Figure 4-6 and the main results are summarized in Figure 4-7. Figure 4-6 shows the cylinder placed at the center of a square domain and the finite element grid surrounding the cylinder. The domain boundaries are periodic on the surface of the cylinder the slip boundary condition (eqn. 4-3 and 4-4) is applied. The flow is driven by a uniform force density applied to the fluid (equivalent to a pressure gradient), and finite element method is used to solve the Navier-Stokes equation. The flow is firstly solved in the no-slip



limit ( $\lambda=0$ ); then, the mean free path is progressively increased to increase the Knudsen number, and the flow velocity increases (the force density remains the same) due to the velocity slip at the surface of the cylinder. The velocity ratio  $V_{\text{slip}}/V_{\text{noslip}}$  is equivalent to the ratio between the apparent permeability and the Darcy permeability  $k_{\text{app}}/k$ , and is presented as a function of cylinder area fraction and the Knudsen number in Figure 4-7. The TMAC is fixed at 0.9. It may be observed that, for this particular geometry, even a moderate Knudsen number would lead to a significant increase in the apparent permeability.

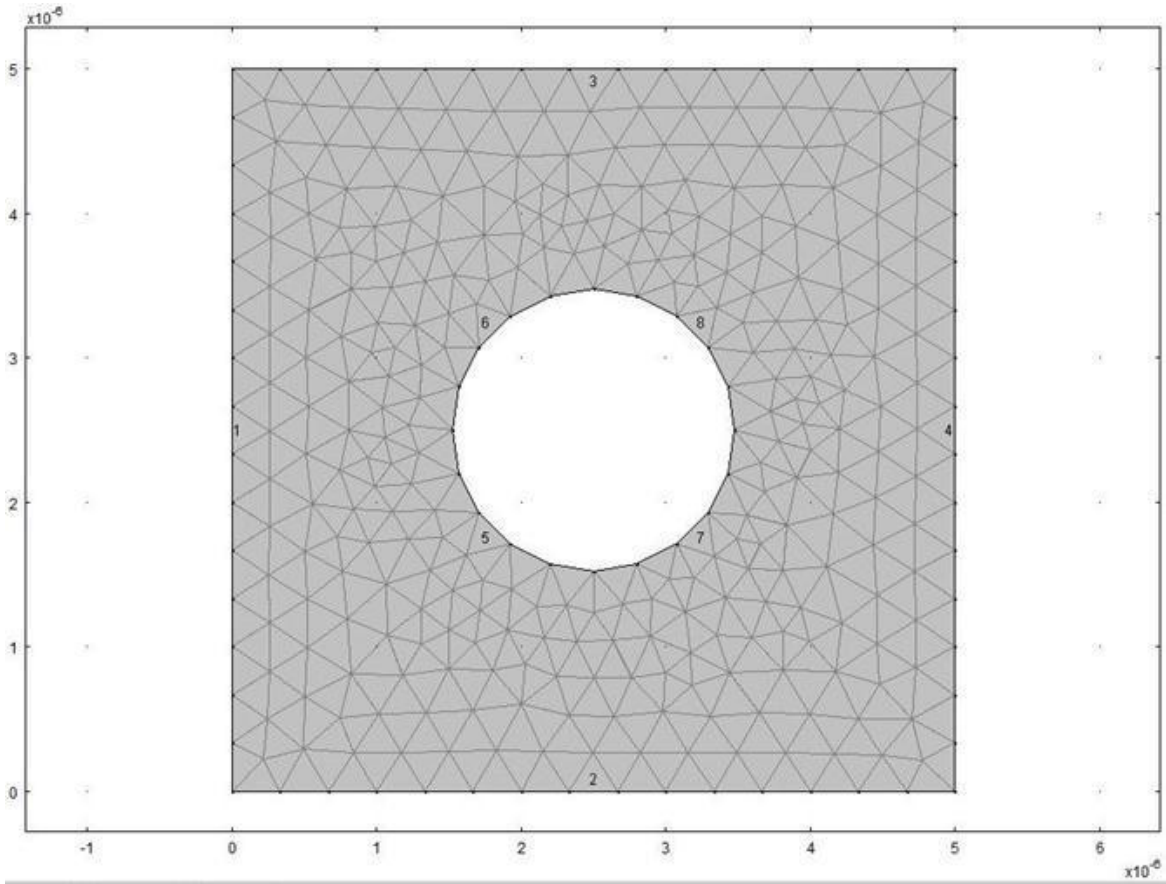


Figure 4-6: A cylinder placed in the center of a square domain for COMSOL simulation and the finite element grid. The force density is applied such that the flow is from left to right. The dimensions are in the unit of micrometers.

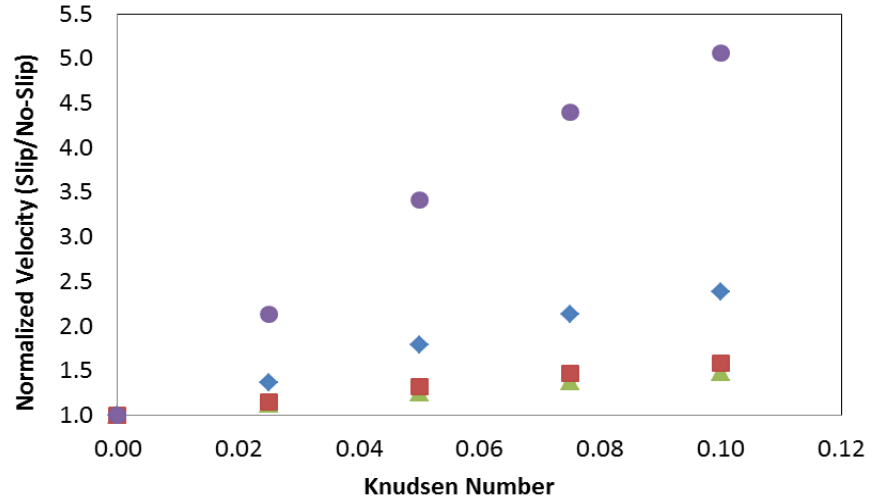


Figure 4-7: Effect of Knudsen number on the ratio/ from COMSOL simulations.

Circles, diamonds, squares, and triangles correspond to cylinder area fraction of 0.299, 0.131, 0.042, and 0.031, respectively.

Effect of slip in fracture, cylinder, and channels with square cross-sections can be derived analytically. For a two-dimensional fracture, the analytical solution predicts that the Klinkenberg coefficient  $b$  in the Klinkenberg law

$$k_{app} = k \left( 1 + \frac{b}{p} \right) \quad (4.5)$$

$b$  should be

$$b = \frac{2 - \sigma}{\sigma} \frac{3\sqrt{2}k_B T}{\pi \delta^2 H} \quad (4.6)$$

Where  $k_B$  is the Boltzmann constant,  $T$  is the temperature,  $\delta$  is the collision diameter of the molecule, and  $H$  is the fracture gap width. For a cylinder, the Klinkenberg coefficient  $b$  is given by

$$b = \frac{2 - \sigma}{\sigma} \frac{2\sqrt{2}k_B T}{\pi \delta^2 R} \quad (4.7)$$

Where  $R$  is the radius of the cylinder. Finally, for a channel with a rectangular cross section, the expression for the permeability in the no-slip limit was derived based on separation of variables

$$k = \frac{L_y^2}{12} \left[ 1 - \sum_{n=1,3,5,\dots}^{\infty} \frac{192L_y}{(n\pi)^5 L_z} \tanh\left(\frac{n\pi L_z}{2L_y}\right) \right] \quad (4.8)$$

And the expression for the permeability in the presence of slip is

$$k_{app} = \frac{L_y^2}{12} + \frac{\lambda L_y}{2} \frac{2-\sigma}{\sigma} + \sum_{i=1}^5 \frac{\left( \frac{L_y}{K_i^*} \cos K_i^* - \frac{L_y}{K_i^{*2}} \sin K_i^* - 2\lambda \frac{2-\sigma}{\sigma} \sin K_i^* \right) \cdot A L_y \cdot \sin K_i^* \cdot \sinh \frac{K_i^*}{A}}{\left[ \sin(2K_i^*) + 2K_i^* \right] \left( \cosh \frac{K_i^*}{A} + \frac{2-\sigma}{\sigma} \frac{2\lambda}{L_y} K_i^* \sinh \frac{K_i^*}{A} \right) \cdot K_i^{*2}} \quad (4.9)$$

In eqs. (4.8) and (4.9),  $L_y$  and  $L_z$  are the dimensions of the channel in the y and z directions, respectively, and  $A=L_y L_z$  is the cross-sectional area of the channel. The eigenvalues  $K_i^*$  is the i-th solution of the transcendental equation

$$\tan K_i^* = \frac{2\sigma}{2-\sigma} \frac{1}{\lambda L_y K_i^*} \quad (4.10)$$

The solution for the velocity profile in a two-dimensional fracture is plotted in Figure 4-8. The solution for the velocity profile in a rectangular channel is plotted in Figure 4-9. The size of the rectangular channel is 100nm (height)  $\times$  5  $\mu$ m (width), identical to the dimension of the nanofluidic channel used in the experiments.

## 4.5 Conclusions and Future Work

The objective of Task 4 is to develop numerical model capability to simulate pore-scale single- and multiphase flow processes, transport of solute, and particulates. The work in the second year focused on simulation of the transport processes and numerical and analytical results for slip flow of gases in simple geometries. In the third year, we will continue to develop pore-scale transport models for solutes and particulates.

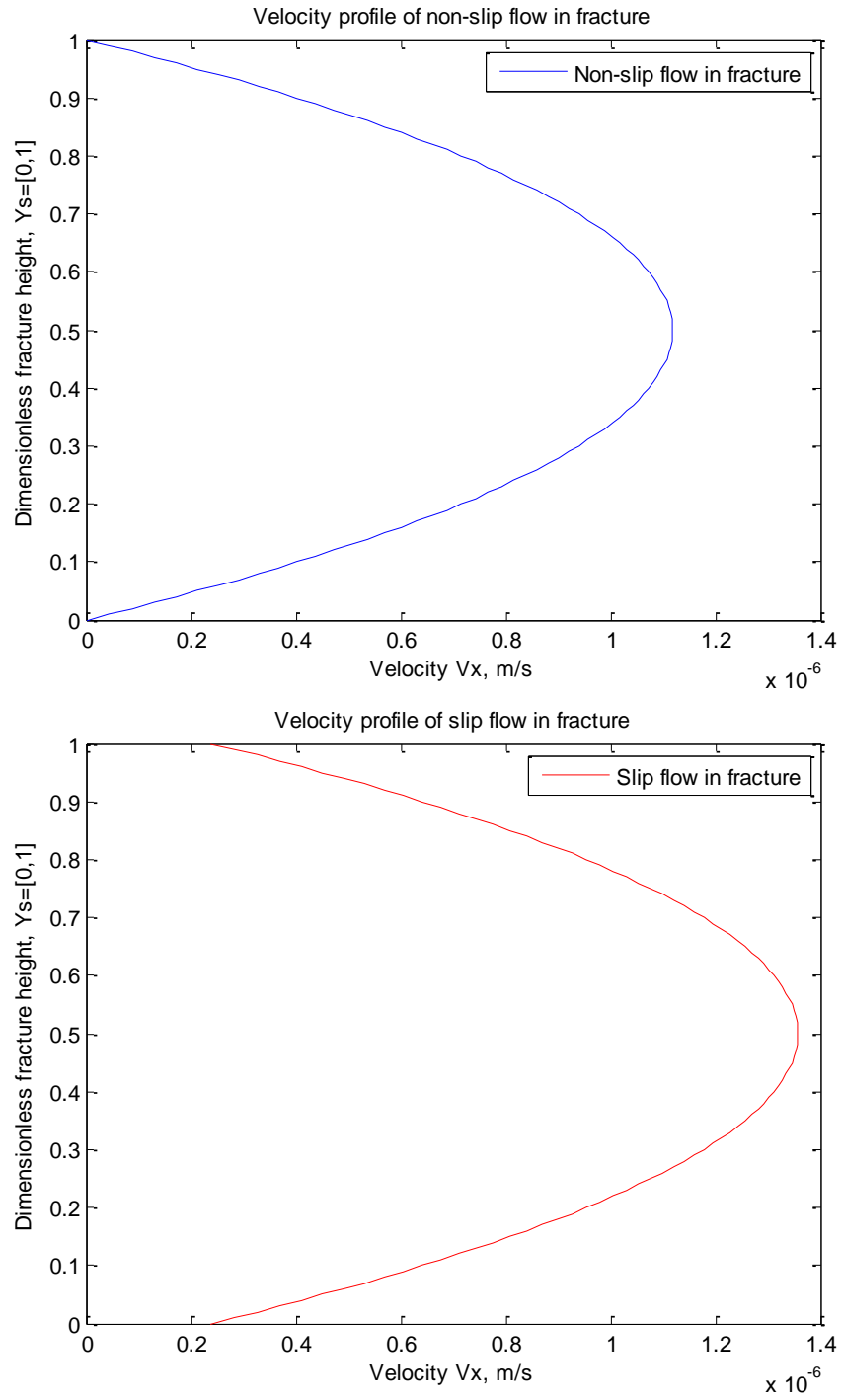


Figure 4-8: Effect of slip on the velocity profile in a 2D Fracture – Analytical solution.

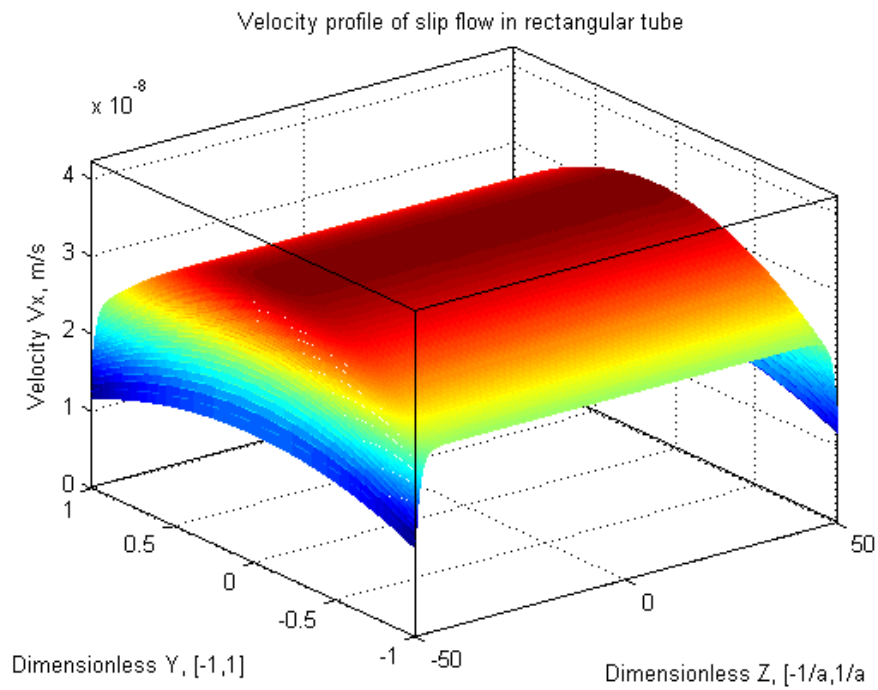
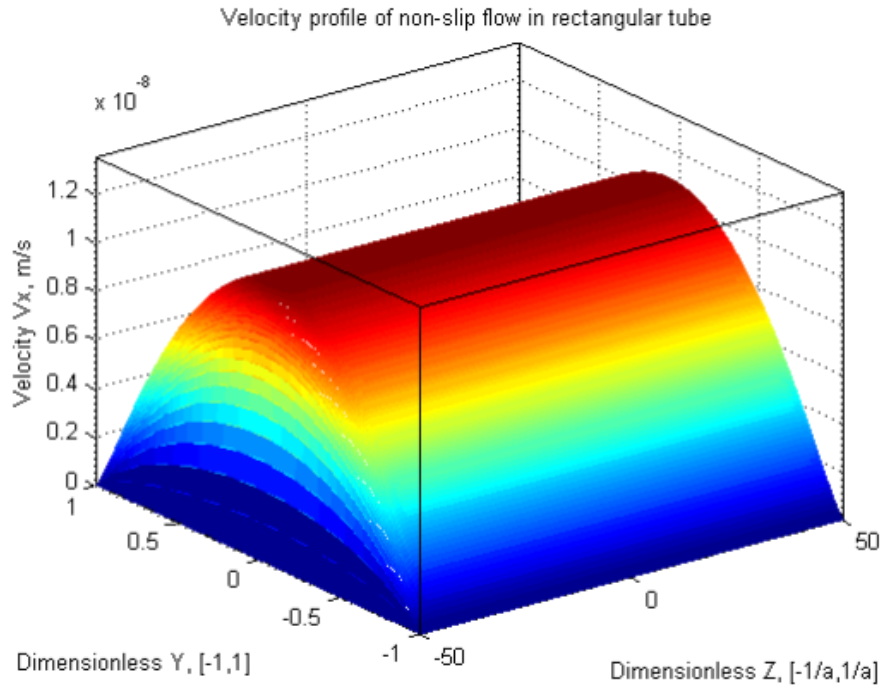


Figure 4-9: Velocity profile of no-slip flow (top) and slip flow (bottom) in a nanofluidic channel (100 nm x 5  $\mu\text{m}$ ).

The following values were used:  $\mu = 1.12 \times 10^{-5} \text{ Pa}\cdot\text{s}$ ,  $r = 53 \text{ nm}$ ,  $\delta = 1$ ,  $\partial p / \partial x = 0.01 \text{ Pa/m}$ .

## 5 Technology Transfer Efforts

### 5.1 Project Website

A project website has been created and is available at:  
([http://web.mst.edu/~baib/Shale%20Gas/RPSEA\\_home.html](http://web.mst.edu/~baib/Shale%20Gas/RPSEA_home.html))

It includes a research summary, lab capability, equipment, publications, and group members.

### 5.2 Full papers

- 1) Wu, Q., OK, JT., Sun, Y., Retterer, S.T., Neeves, K.B., Yin, X., Bai, B., and Ma, Y. (2013). "Optic imaging of single and two-phase pressure-driven flows in nano-scale channels" *Lab chip*. DOI: 10.1039/c2lc41259d.
- 2) Wu, Q., Bai, B., Ma, Y., OK, JT., Neeves, K.B., Yin, X., (2013). "Optic imaging of two-phase flow behavior in nano-scale fractures" SPE 164549, North American Unconventional Resources Conference. The Woodlands, Texas, Society of Petroleum Engineers.
- 3) Sun, Y., Wu, Q., Bai, B., Ma, Y., (2013). "The Flow Behavior of Friction Reducer in Microchannels during Slickwater Fracturing", SPE 164476, SPE Production and Operations Symposium. Oklahoma City, Oklahoma, USA, Society of Petroleum Engineers.
- 4) Sun, Y., Zhang H., Wu, Q., Wei, M., Bai, B., Ma, Y., (2013). "Experimental Study of Friction Reducer Flows in Microfracture during Slickwater Fracturing". SPE 164053, SPE International Symposium on Oilfield Chemistry. Woodlands, Texas, USA, Society of Petroleum Engineers.
- 5) Bai, B.; Elgmati, M.; Zhang, H.; Wei, M. "Rock Characterization of Fayetteville Shale Gas Plays," *Fuel*, March 2013, 105, 645-652
- 6) Zhang, H., Bai, B., Song, K. (2012). "Shale Gas Hydraulic Flow Unit Identification Based on SEM-FIB Tomography", SPE 160143, Annual Technical Conference and Exhibition. San Antonio, Texas, USA, Society of Petroleum Engineers.
- 7) Elgmati, M., Zhang, H., Bai, B., Flori, R., and Qu, Q. (2011). Submicron-Pore Characterization of Shale Gas Plays. SPE 144050, North American Unconventional Gas Conference and Exhibition. The Woodlands, Texas, USA, Society of Petroleum Engineers.
- 8) Elgmati, M., Zobaa, M., Zhang, H., Bai, B., and Oboh-Ikuenobe, F. (2011). Palynofacies Analysis and Submicron Pore Modeling of Shale-Gas Plays. SPE 144267, North American Unconventional Gas Conference and Exhibition. The Woodlands, Texas, USA, Society of Petroleum Engineers.
- 9) Wu, M., Xiao, F., Johnson-Paben, R., Retterer, S., Yin, X., Neeves, K. "Single- and Two- Phase Flow in Microfluidic Porous Media Analogs Based on Voronoi Tessellation," *Lab Chip*, 12:253-261, 2012. The paper is featured on the cover

of the journal

### 5.3 Oral Presentations

- 1) Qihua Wu, Baojun Bai, Yinfa Ma, Jeong Tae Ok, Yongpeng Sun, Xiaolong Yin, Keith Neeves, "Visualization of gas/water two phase flow and displacement of gas/water in nanochannels using single a molecule imaging system", Pittsburgh Conference, March 17 - 21, 2013, Pennsylvania Convention Center, Philadelphia, PA USA
- 2) Yinfa Ma, Qihua Wu, Baojun Bai, Jeong Tae Ok, Yongpeng Sun, Xiaolong Yin, Keith Neeves, "Optical imaging of gas/water two phase flow behavior in nanochannels using single molecule imaging system", 245<sup>th</sup> American Chemical Society National Meeting, New Orleans, Louisiana, April 7-11, 2013.
- 3) Hao Zhang, Baojun Bai, Kai Song. "Shale Gas Hydraulic Flow Unit Identification Based on SEM-FIB Tomography", paper SPE 160143 presented at the SPE Annual Technical Conference and Exhibition held in San Antonio, Texas, USA, 8-10 October 2012.
- 4) Bai, B., Yin, X.; Ma, Y. "Using Single-molecule Imaging System Combined with Nano- fluidic Chips to Understand Fluid Flow in Tight and Shale Gas Formation," Digital Rock International Conference, Qingdao, China, 7-8 June, 2012.
- 5) Bai, B. "Gas Flow in Nano-Scale Porous Media," Shell Company," Beijing, June 2012, invited talk.
- 6) Bai, B. "Using Single-molecule Imaging System Combined with Nano-fluidic Chips to Understand Fluid Flow in Tight and Shale Gas Formation," Conoco-Phillips, Houston, TX, Sept 2012, invited talk.
- 7) Bai, B. "Characterization of Shale Gas Rocks," Langfang Branch of Research Institute of Petroleum Exploration and Development, PetroChina, Langfang, Hebei, China, Aug 4, 2011, invited talk
- 8) Yin, X. "Pore-scale numerical simulation and microfluidic / nanofluidic physical models," International Workshop on Digital Core Analysis Technology, Qingdao, China, June 2012.
- 9) Yin, X. "Numerical and Laboratory Study of Gas Flow through Unconventional Reservoir Rocks," oral presentation at RPSEA Piceance Basin Tight Gas Research Review meeting, April 21, 2011, Denver, Colorado, USA.
- 10) Elgmati, M., Zhang, H., Bai, B., Flori, R., and Qu, Q. Submicron-Pore Characterization of Shale Gas Plays. North American Unconventional Gas Conference and Exhibition. June 14, 2011, The Woodlands, Texas, USA, Society of Petroleum Engineers.
- 11) Elgmati, M., Zobaa, M., Zhang, H., Bai, B., and Oboh-Ikuenobe, F. Palynofacies Analysis and Submicron Pore Modeling of Shale-Gas Plays. North American Unconventional Gas Conference and Exhibition. June 14, 2011, The Woodlands, Texas, USA, Society of Petroleum Engineers.
- 12) Neeves, K. "Micro- and nanoscale porous media analogs for studying multiphase flow," invited presentation at the ORNL Center for Nanophase

Materials Science User Meeting, September 9, 2011, Oak Ridge, TN.

- 13) Xiao, F., and Yin, X. "Porosity-Permeability Relations in Granular, Fibrous, and Tubular Geometries," oral presentation at American Physical Society, Division of Fluid Dynamics meeting, November 21, 2011, Baltimore, Maryland, USA.

## 5.4 Posters

- 1) Yin, X. Visualization of water flooding and formation damage in micro- and nanofluidic porous media analogs, Gordon Research Conference – Flow and Transport in Porous Media, Les Diablerets, Switzerland.
- 2) Yin, X. Micromodel study of influence of pore geometry on water-oil displacement with and without surfactant, American Geophysical Union, Fall Meeting 2012, San Francisco, California, USA. Cheng, X., Wu, Q. Bai, B., Ma, Y. Velocity Profiling of polymer/aqueous phase interface in microchannel using single molecule imaging system, Poster at Pittcon, March 13, 2011, Atlanta, Georgia, USA.
- 3) Qihua Wu, , Yongpeng Sun, Baojun Bai, Yinfa Ma, "Investigation of Flow Behavior of Polymer/Gas and Surfactant/Gas Two phase Fluids in Microchannel Using Single Molecule Imaging System", Pittsburgh Conference, Orlando, FL, March 11-15, 2012.
- 4) Xiaoliang Cheng, Qihua Wu, Baojun Bai and Yinfa Ma, "Investigation of gas flow in nanochannels and polymer effect on the gas flow using single molecule imaging system". Pittsburgh Conference, Atlanta, GA, March 13-18, 2011.

## 5.5 Graduate thesis

- 1) (MS thesis) Xu W, Effect of Pore Geometry on Water and Surfactant Flooding by PDMS Microfluidic Micromodels, Colorado School of Mines, 2012.
- 2) (MS thesis) Gbededo M, Pore-Scale Study on Slip Flow of Gas in Porous Media, Colorado School of Mines, 2012.
- 3) (MS thesis) Malek Elgmati, Shale Gas Characterization, Missouri University of Science and Technology, 2011.



## REFERENCES

1. Salles J, Thovert JF, Delannay R, Prevors L, Auriault JL, Adler PM, Taylor dispersion in porous media – determination of the dispersion tensor, *Phys. Fluids A*, 1993. **5**:2348-2376.
2. Neeves, K.B., et al., Fabrication and characterization of microfluidic probes for convection enhanced drug delivery. *J. Controlled Release*, 2006. **111**(3): p. 252-262.
3. Chung, A.J., D. Kim, and D. Erickson, Electrokinetic microfluidic devices for rapid, low power drug delivery in autonomous microsystems. *Lab on a Chip*, 2008. **8**(2): p. 330-338.
4. Shestopalov, I., J.D. Tice, and R.F. Ismagilov, Multi-step synthesis of nanoparticles performed on millisecond time scale in amicrofluidic droplet- based system. *Lab on a Chip*, 2004. **4**: p. 316-321
5. Kaban'kov, O.N. and A.P. Sevast'yanov, Two-phase flows: a review. *Heat Transfer Res*, 2000. **31**: p. 103-122.
6. Berejnov, V., N. Djilali, and D. Sinton, Lab-on-chip methodologies for the study of transport in porous media: energy applications. *Lab on a Chip*, 2008. **8**: p. 689-683.
7. Chen, X.Y., et al., Developing pressure-driven liquid flow in microchannels under the electrokinetic effect. *International Journal of Engineering Science*, 2004. **42**: p. 609-622.
8. Dutta, D., A. Ramachandran, and D.T.L. Jr, Effect of channel geometry on solute dispersion in pressure-driven microfluidic systems. *Microfluid Nanofluid*, 2006. **2**: p. 275-290.
9. Lauga, E. and H.A. Stone, Effective slip in pressure-driven Stokes flow. *J. Fluid Mech*, 2003. **489**: p. 55-77.
10. Tamaki, E., et al., Pressure-driven flow control system for nanofluidic chemical process. *Journal of Chromatography A*, 2006. **1137**: p. 256-262.
11. Ward, T., et al., Microfluidic flow focusing: Drop size and scaling in pressure versus flow-rate-driven pumping. *Electrophoresis*, 2005. **26**: p. 3716-3724.
12. Raghu, R.C. and J. Schofield, Simulation of Pressure-Driven Flows in Nanochannels Using Multiparticle Collision Dynamics. *J. Phys. Chem. C*, 2010. **114**: p. 20659-20671.
13. Serizawa, A., Z. Feng, and Z. Kawara, Two-phase flow in microchannels. *Experimental Thermal and Fluid Science* 2002. **26**: p. 703-714.
14. Mandhane, J.M., G.A. Gregory, and K. Aziz, A flow pattern map for gas-liquid flow in horizontal pipes. *Int. J. Multiphase Flow*, 1974. **1**(4): p. 537-553.
15. Travis, K.P., B.D. Todd, and D.J. Evans, Departure from Navier-Stokes hydrodynamics in confined liquids. *Physical Review E*, 1997. **55**(4): p. 4288- 4295.
16. Cheng, J.T. and N. Giordano, Fluid flow through nanometer-scale channels. *Physical Review E*, 2002. **65**: p. 031206.

17. Hibara, A., et al., Nanochannels on a Fused-Silica Microchip and Liquid Properties Investigation by Time-Resolved Fluorescence Measurements. *Anal. Chem*, 2002. **74**(24): p. 6170-6176.
18. Cuenca, A. and H. Bodiguel, Fluorescence photobleaching to evaluate flow velocity and hydrodynamic dispersion in nanoslits. *Lab on a Chip*, 2012. **12**: p. 1672-1679.
19. Sinton, D., Microscale flow visualization. *Microfluidic And Nanofluidic*, 2004. **1**(1): p. 2-21.
20. Gai, H., et al., Simultaneous measurements of the flow velocities in a microchannel by wide/evanescent field illuminations with particle/single molecules. *Lab on a Chip*, 2005. **5**(5): p. 443-449.
21. Gai, H., et al., Correlations between Molecular Numbers and Molecular Masses in an Evanescent Field and Their Applications in Probing Molecular Interactions. *Angewandte Chemie*, 2005. **117**(32): p. 5237-5240.
22. Banerjee, A., et al., Concentration dependence of fluorescence signal in a microfluidic fluorescence detector. *Journal of Luminescence*, 2010. **130**: p. 1095-1100.
23. Penzkofer, A. and W. Leupacher, S0-S1 two photon absorption dynamics of organic dye solutions. *Optical and Quantum Electronic*, 1987. **19**(6): p. 327- 349.
24. Bindhu, C.V., et al., Measurement of the absolute fluorescence quantum yield of rhodamine B solution using a dual-beam thermal lens technique. *Journal of Physics D: Applied Physics*, 1996. **29**(4): p. 1074-109.
25. Qi, D., D.J. Hoelzle, and A.C. Rowat, Probing single cells using flow in microfluidic devices. *The European Physical Journal*, 2012. **204**: p. 85-101.
26. Tas, N.R., et al., Capillary filling speed of water in nanochannels. *Applied Physics Letters*, 2004. **85**(15): p. 3274-3276.
27. Elazhary, A.M. and H.M. Soliman, Two-phase flow in a horizontal mini-size impacting T-junction with a rectangular cross-section. *International Journal of Multiphase Flow*, 2012. **42**: p. 104-113.
28. Yang, Z.C., et al., Nitrogen/non-Newtonian fluid two-phase upward flow in non-circular microchannels. *International Journal of Multiphase Flow*, 2010. **36**: p. 60-70.
29. Kawahara, A., P.M.-Y. Chung, and M. Kawaji, Investigation of two-phase flow pattern, void fraction and pressure drop in a microchannel. *International Journal of Multiphase Flow*, 2002. **28**: p. 1411-1435.
30. Saisorn, S. and S. Wongwises, The effects of channel diameter on flow pattern, void fraction and pressure drop of two-phase air–water flow in circular micro-channels. *Experimental Thermal and Fluid Science*, 2010. **34**: p. 454-462.
31. Ide, H., A. Kariyasaki, and T. Fukano, Fundamental data on the gas-liquid twophase flow in Minichannels. *Int. J. Thermal Sci*, 2007. **46**: p. 519-530.
32. Hibiki, T. and K. Mishima, Flow regime transition criteria for upward two- phase flow in vertical narrow rectangular channels. *Nuclear Engineering and Design*, 2001. **203**: p. 117-131.
33. Javadpour, F., Nanopores and apparent permeability of gas flow in mudrocks (shales

- and siltstone). *Journal of Canadian Petroleum Technology*, 2009. **48**(8): p. 16-21.
34. Javadpour, F., D. Fisher, and M. Unsworth, Nanoscale gas flow in shale gas sediments. *Journal of Canadian Petroleum Technology*, 2007. **46**(10).
  35. Xiong, X., et al. A Fully-Coupled Free and Adsorptive Phase Transport Model for Shale Gas Reservoirs Including Non-Darcy Flow Effects. in *SPE Annual Technical Conference and Exhibition*. 2012.
  36. Swami, V., C. Clarkson, and A. Settari. Non-Darcy Flow in Shale Nanopores: Do We Have a Final Answer? in *SPE Canadian Unconventional Resources Conference*. 2012.
  37. Jones, F.O. and W. Owens, A laboratory study of low-permeability gas sands. *Journal of Petroleum Technology*, 1980. **32**(9): p. 1631-1640.
  38. Fulton, P.F., The effect of gas slippage on relative permeability measurements. *Producers Monthly*, 1951. **15**(12): p. 14-19.
  39. Li, K. and R. Horne, Experimental study of gas slippage in two-phase flow. *SPE Reservoir Evaluation & Engineering*, 2004. **7**(6): p. 409-415.
  40. Qingjie, L., et al. The effect of water saturation on gas slip factor by pore scale network modeling. in *SCA 2002 Symposium*, Monterey, California, September. 2002.
  41. Rose, W.D., Permeability and gas-slippage phenomena. 28 th Annual Mtg. Topical Committee on Production Technology, 1948.
  42. Rushing, J., K. Newsham, and K. Fraassen. Measurement of the two-phase gas slippage phenomenon and its effect on gas relative permeability in tight gas sands. in *SPE Annual Technical Conference and Exhibition*. 2003.
  43. Sampath, K. and C. Keighin, Factors affecting gas slippage in tight sandstones of cretaceous age in the Uinta basin. *Journal of Petroleum Technology*, 1982. **34**(11): p. 2715-2720.
  44. Wan, J. and J.L. Wilson, Visualization of the role of the gas-water interface on the fate and transport of colloids in porous media. *Water Resources Research*, 1994. **30**(1): p. 11-24.
  45. Lanning, L.M. and R.M. Ford, Glass micromodel study of bacterial dispersion in spatially periodic porous networks. *Biotechnology and bioengineering*, 2002. **78**(5): p. 556-566.
  46. Javadpour, F. and D. Fisher, Nanotechnology-based micromodels and new image analysis to study transport in porous media. *Journal of Canadian Petroleum Technology*, 2008. **47**(2).
  47. Wu, M., et al., Single-and two-phase flow in microfluidic porous media analogs based on Voronoi tessellation. *Lab on a Chip*, 2012. **12**(2): p. 253- 261.
  48. Romero-Zeron, L. and A. Kantzas, The effect of wettability and pore geometry on foamed-gel-blockage performance. *SPE Reservoir Evaluation & Engineering*, 2007. **10**(2): p. 150-163.
  49. Klinkenberg, L., The permeability of porous media to liquids and gases. *Drilling and production practice*, 1941.
  50. Schaaf, S. A. & Chambre, P. L. Flow of rarefied gases. Princeton University Press, 1961. New Jersey.
  51. Dullien, F.A.L., Porous media: fluid transport and pore structure. Vol. 2. 1992:

Academic press San Diego.

52. King, G.E., Thirty Years of Gas Shale Fracturing: What Have We Learned?, in SPE Annual Technical Conference and Exhibition. 2010, Society of Petroleum Engineers: Florence, Italy.
53. Apaydin, O.G., E. Ozkan, and R. Raghavan, Effect of Discontinuous Microfractures on Ultratight Matrix Permeability of a Dual-Porosity Medium. SPE Reservoir Evaluation & Engineering, 2012. **15**(4): p. pp. 473-485.
54. Wang, F.P., Production Fairway: Speed Rails in Gas Shales, in 7th Annual Gas Shales Summit. 2008: Dallas, TX.
55. Ding, W., et al., Fracture development in shale and its relationship to gas accumulation. Geoscience Frontiers, 2012. **3**(1): p. 97-105.
56. Grieser, B., et al., The Rocket Science Behind Water Frac Design, in SPE Production and Operations Symposium. 2003, Society of Petroleum Engineers Inc.: Oklahoma City, Oklahoma.
57. Palisch, T., M. Vincent, and P. Handren, Slickwater Fracturing: Food for Thought. SPE Production & Operations, 2010. **25**(3): p. 327-344.
58. Ram, A., E. Finkelstein, and C. Elata, Reduction of Friction in Oil Pipelines by Polymer Additives. Industrial & Engineering Chemistry Process Design and Development, 1967. **6**(3): p. 309-313.
59. White, C.M. and M.G. Mungal, Mechanics and Prediction of Turbulent Drag Reduction with Polymer Additives. Annual Review of Fluid Mechanics, 2008. **40**: p. 235-256.
60. Shah, S.N. and A.H.A. Kamel, Investigation of Flow Behavior of Slickwater in Large Straight and Coiled Tubing. SPE Production & Operations, 2010. **25**(1): p. 70-79.
61. Rimassa, S.M., P. Howard, and M.O. Arnold, Are You Buying Too Much Friction Reducer Because of Your Biocide?, in SPE Hydraulic Fracturing Technology Conference. 2009, Society of Petroleum Engineers: The Woodlands, Texas.
62. Kaufman, P.B., G.S. Penny, and J. Paktinat, Critical Evaluation of Additives Used in Shale Slickwater Fracs, in SPE Shale Gas Production Conference. 2008, Society of Petroleum Engineers: Fort Worth, Texas, USA.
63. Rimassa, S.M., P.R. Howard, and K.A. Blow, Optimizing Fracturing Fluids From Flowback Water, in SPE Tight Gas Completions Conference. 2009, Society of Petroleum Engineers: San Antonio, Texas, USA.
64. Zelenev, A.S., G.A. Gilzow, and P.B. Kaufman, Fast Inverting, Brine and Additive Tolerant Friction Reducer for Well Stimulation, in SPE International Symposium on Oilfield Chemistry. 2009, Society of Petroleum Engineers: The Woodlands. Texas.
65. Paktinat, J., et al., Critical Evaluation of High Brine Tolerant Additives Used in Shale Slick Water Fracs, in SPE Production and Operations Symposium. 2011, Society of Petroleum Engineers: Oklahoma City, Oklahoma, USA.
66. Baser, B., et al., An Alternative Method of Dealing With Pressure: Friction Reducer for Water Packing of Long Horizontal Open Holes in Low- Fracturing-Gradient Environments. SPE Drilling & Completion, 2010. **25**(3): p. 300-308.
67. Sun, H., et al., A Nondamaging Friction Reducer for Slickwater Frac Applications, in SPE Hydraulic Fracturing Technology Conference. 2011: The Woodlands, Texas,

USA.

68. Lindsay, S.D., et al., Use of Salt-Tolerant Friction Reducer for Coiled-Tubing Applications in Unconventional Shale Formations, in SPE/ICoTA Coiled Tubing & Well Intervention Conference and Exhibition. 2011, Society of Petroleum Engineers: The Woodlands, Texas, USA.
69. Paktinat, J., B.J. O'Neil, and M.G. Tulissi, Case Studies: Impact of High Salt Tolerant Friction Reducers on Freshwater Conversation in Canadian Shale Fracturing Treatments, in Canadian Unconventional Resources Conference. 2011, Society of Petroleum Engineers: Alberta, Canada.
70. Sun, H., et al., A Novel Nondamaging Friction Reducer: Development and Successful Slickwater Frac Applications, in Tight Gas Completions Conference. 2010, Society of Petroleum Engineers: San Antonio, Texas, USA.
71. Zhou, J., et al., Bridging the Gap between Laboratory Characterization and Field Applications of Friction Reducers, in SPE Production and Operations Symposium. 2011: Oklahoma City, Oklahoma, USA.
72. Odusina, E.O., C.H. Sondergeld, and C.S. Rai, An NMR Study of Shale Wettability, in Canadian Unconventional Resources Conference. 2011, Society of Petroleum Engineers: Alberta, Canada.
73. Krishnamoorthy, C. and A.J. Ghajar, Single-Phase Friction Factor in Micro- Tubes: A Critical Review of Measurement, Instrumentation and Data Reduction Techniques From 1991-2006, in ASME 2007 5th International Conference on Nanochannels, Microchannels, and Minichannels. 2007, ASME: Puebla, Mexico
74. Celata, G., et al., Characterization of Fluid Dynamic Behaviour and Channel Wall Effects In Microtube. International Journal of Heat and Fluid Flow, 2006. **27**(1): p. 135-143.
75. Wang, F., et al., Influence of Wettability on Flow Characteristics of Water through Microtubes and Cores. Chinese Science Bulletin, 2009. **54**(13): p. 2256-2262.
76. Henares, T.G., et al., "Drop-and-Sip" Fluid Handling Technique for the Reagent-Release Capillary (RRC)-based Capillary-Assembled Microchip (CAS- CHIP): Sample Delivery Optimization and Reagent Release Behavior in RRC. Analytical Sciences, 2008. **24**(1): p. 127-132.
77. Song, F.-Q., J.-D. Wang, and H.-L. Liu, Static Threshold Pressure Gradient Characteristics of Liquid Influenced by Boundary Wettability. Chinese Physics Letters, 2010. **27**: p. 024704.
78. Hjertén, S. and M. Kiessling-Johansson, High-Performance Displacement Electrophoresis in 0.025-To 0.050-Mm Capillaries Coated With a Polymer To Suppress Adsorption And Electroendosmosis. Journal of Chromatography A, 1991. **550**: p. 811-822.
79. Seright, R., et al., New Insights into Polymer Rheology in Porous Media. SPE Journal, 2011. **16**(1): p. 35-42.
80. Bitsch, L., Blood flow in microchannels, in Master's thesis. 2002, Denmark Technical University.
81. Zhang, H. and B. Bai, Preformed-Particle-Gel Transport Through Open Fractures and

- Its Effect on Water Flow. SPE Journal, 2011. **16**(2): p. 388-400.
82. Zhao, J.Z., et al., Influences of Fracture Aperture on the Water-Shutoff Performance of PEI Cross-Linking HPAM Gels in Hydraulic Fractured Reservoirs. Energy & Fuels, 2011. **25**(6): p. 2616-2624.
  83. Seright, R., Gel Placement in Fractured Systems. SPE Production & Facilities, 1995. **10**(4): p. 241-248.
  84. Ge, J. and A. Ghassemi, Permeability Enhancement In Shale Gas Reservoirs After Stimulation By Hydraulic Fracturing, in 45th U.S. Rock Mechanics / Geomechanics Symposium. 2011, American Rock Mechanics Association: San Francisco, California.
  85. Weng, X., et al., Modeling of Hydraulic-Fracture-Network Propagation in a Naturally Fractured Formation. SPE Production & Operations, 2011. **26**(4): p. pp. 368-380.
  86. Gasparik, M., et al., High-Pressure Methane Sorption Isotherms of Black Shales from the Netherlands. Energy & Fuels, 2012. **26**(8): p. 4995-5004.
  87. Ambrose, R., et al., Shale Gas-in-Place Calculations Part I: New Pore-Scale Considerations. SPE Journal, 2012. **17**(1): p. 219-229.
  88. Elgmami, M.M., et al., Submicron-Pore Characterization of Shale Gas Plays, in North American Unconventional Gas Conference and Exhibition. 2011, Society of Petroleum Engineers: The Woodlands, Texas, USA.
  89. Leahy-Dios, A., et al., Modeling of Transport Phenomena and Multicomponent Sorption for Shale Gas and Coalbed Methane in an Unstructured Grid Simulator, in SPE Annual Technical Conference and Exhibition. 2011, Society of Petroleum Engineers: Denver, Colorado, USA.
  90. Nelson, P.H., Pore-Throat Sizes in Sandstones, Tight Sandstones, and Shales. AAPG bulletin, 2009. **93**(3): p. 329.
  91. Wang LY, Koch DL, Yin XL, Cohen C, Hydrodynamic diffusion and mass transfer across a sheared suspension of neutrally buoyant spheres, Phys Fluids, 2009. 21:033303.
  92. Szymczak P, Ladd AJC, Stochastic boundary conditions to the convective- diffusion equation including chemical reactions at solid surfaces, Phys. Rev. E, 2004. 69:036704.
  93. Ladd AJC, Verberg R, Lattice-Boltzmann simulations of particle-fluid suspensions, J. Stat. Phys, 2001. 104:1191.
  94. Nguyen NQ, Ladd AJC, Lubrication correction for lattice-Boltzmann simulations of particle suspensions, Phys. Rev. E, 2002. 66:046708.
  95. Metzger B, Rahli O, Yin XL, Heat transfer across sheared suspensions: role of the shear-induced diffusion, submitted to J. Fluid Mech.2012
  96. Ginzburg I, Equilibrium-type and link-type lattice Boltzmann models for generic advection and anisotropic-dispersion equation, Adv. Water Resour. 2005, 28:1171-1195.
  97. Ginzburg I, Generic boundary conditions for lattice Boltzmann models and their applications to advection and anisotropic dispersion equations, Adv. Water Resour. 2005, 28:1196-1216
  98. Sondergeld CH, Newsham KE, Comisky JT, Rice MC, Rai CS, Petrophysical

- considerations in evaluating and producing shale gas, 2010. SPE 131768.
99. Elgmati M, Zhang H, Bai BJ, Flori R, Qu Q, Submicron-pore characterization of shale gas plays, 2011. SPE 144050.
100. Knackstedt M, Golab A, Riepe L, Petrophysical characterization of unconventional reservoir core at multiple scales, SPWLA 53rd Annual Logging Symposium, 2012.

## **LIST OF ACRONYMS AND ABBREVIATIONS**

XRD: X-ray

Diffraction Bcf:

billion cubic feet Tcf:

trillion cubic feet

EIA: US Energy Information

Administration USGS: United States

Geological Survey DIW: deionized water

TOC: Total organic carbon

SEM/FIB: Focused ion beam/scanning electron microscope

PDMS: Polydimethylsiloxane